INTERIM REPORT

Three-dimensional Computational Modeling of Turbulent Flow Field, Bed Morphodynamics and Liquefaction Adjacent to Munitions

SERDP Project MR-2732

JULY 2019

Xiaofeng Liu
Tong Qiu
The Pennsylvania State University

SERDP
DOD ▪ EPA ▪ DOE

REPORT DOCUMENTATION PAGE

Form Approved
OMB No. 0704-0188

1. REPORT DATE *(DD-MM-YYYY)*	**2. REPORT TYPE**	**3. DATES COVERED** *(From - To)*
31/07/2019	SERDP Interim Report	7/28/2017 - 7/28/2022

4. TITLE AND SUBTITLE

Three-dimensional Computational Modeling of Turbulent Flow Field, Bed Morphodynamics and Liquefaction Adjacent to Munitions

5a. CONTRACT NUMBER
17-C-0041

5b. GRANT NUMBER

5c. PROGRAM ELEMENT NUMBER

6. AUTHOR(S)
Xiaofeng Liu
Tong Qiu

5d. PROJECT NUMBER
MR-2732

5e. TASK NUMBER

5f. WORK UNIT NUMBER

7. PERFORMING ORGANIZATION NAME(S) AND ADDRESS(ES)
The Pennsylvania State University
110 Technology Center Building
University Park, PA 16802

8. PERFORMING ORGANIZATION REPORT NUMBER
MR-2732

9. SPONSORING/MONITORING AGENCY NAME(S) AND ADDRESS(ES)
Strategic Environmental Research and Development Program (SERDP)
4800 Mark Center Drive, Suite 16F16
Alexandria, VA 22350-3605

10. SPONSOR/MONITOR'S ACRONYM(S)
SERDP

11. SPONSOR/MONITOR'S REPORT NUMBER(S)
MR-2732

12. DISTRIBUTION/AVAILABILITY STATEMENT
DISTRIBUTION STATEMENT A. Approved for public release: distribution unlimited.

13. SUPPLEMENTARY NOTES

14. ABSTRACT
This project addresses directly to the research need outlined in MRSON-17-01 on the topic of “Characteristics of Munitions Underwater and Their Environment”. Large amount of observational and empirical data has been gathered in field and laboratory studies to reveal the mechanisms behind the motion of munitions. However, there are still knowledge gaps for the physical and deterministic explanation of the phenomenology. Our project aims to develop and utilize a three-dimensional (3D) computational model to predict the initiation of motion, continuous movement, and final deposition of munitions, which are important for site assessment and remediation actions. The 3D model captures the key physical processes which control the motion of munitions, including turbulent flow, sediment transport and scour, granular material dynamics, and the rigid-body motion of munitions. In addition, these processes are coupled and thus the developed model should be capable of simulating their interactions.

15. SUBJECT TERMS
Munition Motion, Computational Fluid Dynamics, Immersed Boundary Method, Sediment Scour, Sand Slide, Smoothed Particle Hydrodynamics, Visco-elastoplastic Model

16. SECURITY CLASSIFICATION OF:			**17. LIMITATION OF ABSTRACT**	**18. NUMBER OF PAGES**	**19a. NAME OF RESPONSIBLE PERSON**
a. REPORT	**b. ABSTRACT**	**c. THIS PAGE**			Xiaofeng Liu
UNCLASS	UNCLASS	UNCLASS	UNCLASS	64	**19b. TELEPHONE NUMBER** *(Include area code)* 814-863-2940

TABLE OF CONTENTS

LIST OF FIGURES

LIST OF TABLES

LIST OF ACRONYMS

1D - One-dimensional

2D - Two-dimensional

3D - Three-dimensional

ALE - Arbitrary-Lagrangian-Eulerian

CFD - Computational Fluid Dynamics

CFL - Courant-Friedrichs-Lewy

DBS - Dynamic Boundary Conditions

DoF - Degrees of freedom

DP - Drucker-Prager

EOS - Equation of State

GPU - Graphics Processing Unit

HBP - Herschel-Bulkley-Papanastasiou

IB - Immersed Boundary

MR - Munition Response

MRSON - Munition Response Statement of Need

RANS - Reynolds Averaged Navier-Stokes

SERDP - Strategic Environmental Research and Development Program

SPH - Smoothed Particle Hydrodynamics

UXO - Unexploded Ordnance

LIST OF SYMBOLS

$\mathbf{A}$ = stencil Matrix

a = aspect ratio

b = reference height for suspended sediment

C = volumetric suspended sediment concentration

C_b = sediment concentration near the bed ($z = b$)

C_{ijk} = polynomial coefficients

$\mathbf{c}$ = coefficients vector

c = cohesion of the sediment

Co_{min} = minimum Courant number

C_{s0} = speed of sound

C_μ = coefficient for wall model

c_v = concentration in volume fraction

D = deposition rate

d = sediment grain diameter

D_d = kinematic eddy diffusivity of suspended sediment

E = entrainment rate

E_y = Young's modulus

$\tilde{E}$ = dimensionless entrainment rate

f = net force acting on each particle on solid boundary

f_i = force per unit mass of particle i

$f(x)$ = field function

g = gravity constant

H = channel depth

h = smoothing length

$\mathbf{I}$ = identity matrix

I = moment of inertia

j_{sat} = yielded saturated sediment particles

$J^{\alpha\beta}$ = Jaumann rate

J_2 = the second invariant of the deviatoric shear stress tensor

K = sand slide diffusivity

k = turbulence kinetic energy

K_0 = sand slide diffusivity constant

k_s, k_s^+ = dimensional and dimensionless roughness height

M = mass of object

$\tilde{m}$ = index for the exponential growth of stress

$\mathbf{n}$ = normal direction vector

n = bed porosity

$\tilde{n}$ = power-law index that enables simulation of shear thinning or shear thickening behavior

p = pressure

P_k = generation rate

$\mathbf{q}$ = sand slide flux vector

q_0 = bedload transport rate for flat horizontal bed

$\mathbf{q}_b$ = bedload transport rate vector

q^* = dimensionless bed-load transport rate

R = submerged specific gravity of sediment

Re = Reynolds number

$\mathbf{R}_0$ = center of object

r_0, h_0 = radius and height of sand cylinder

t = time

U = mean velocity

$\mathbf{u}$ = flow velocity vector

u, v, w = flow velocity components

u_τ = shear velocity

$\mathbf{V}_b$ = velocity of rigid-body

v_s = sediment settling velocity

$w_0, \mathbf{W}$ = weight function, weight function matrix

$W(\mathbf{x} - \mathbf{x}', h)$ = kernel function

x, y, z = Cartesian coordinates

$\tilde{x}, \tilde{y}, \tilde{z}$ = local coordinates

y^+ = dimensionless wall distance

z_b = bed elevation

$\alpha, \beta, \beta^*, \sigma, \sigma^*$ = coefficients for turbulence model

β_1 = angle of local bed

β_2 = angle between local flow velocity and bed slope

δ = distance between a stencil cell center and the corresponding hit point

$\delta^{\alpha\beta}$ = Kronecker's delta function

ϵ = specific dissipation rate

$\dot{\epsilon}_i^{\alpha\beta}$ = deviatoric strain rate

γ = polytropic index

$\theta, \theta_c, \theta_{c0}$ = Shields number, critical Shields numbers for sloped and flat bed

μ = dynamic viscosity

μ_s = static friction coefficient

μ_{app} = apparent viscosity

μ_{susp} = suspension viscosity

ν = fluid kinematic viscosity

ν_p = Poisson's ration

ν_t = turbulence viscosity

$\mathbf{\Omega}_b$ = rotational velocity

$\dot{\omega}_i^{\alpha\beta}$ = spin-rate tensor

ρ = density of water

ρ_0 = reference density

$\sigma^{\alpha\beta}$ = total shear stress tensor

$\tilde{\phi}$ = polynomial function

ϕ_0 = angle of repose

$\boldsymbol{\tau}$ = Reynolds stress vector

$\boldsymbol{\tau}_b$, τ_b = bed-shear stress vector, bed-shear stress

τ_c = yield stress

τ_y = Bingham yield stress

$\tau_i^{\alpha\beta}$ = viscous stress

$\dot{\tau}^{\alpha\beta}$ = deviatoric stress rate

τ_w = wall shear stress

I_1 = the first invariant of the deviatoric shear stress tensor

II_D = the second invariant of the deviatoric strain rate tensor

KEYWORDS

Munition Motion, Computational Fluid Dynamics, Immersed Boundary Method, Sediment Scour, Sand Slide, Smoothed Particle Hydrodynamics, Visco-elastoplastic Model

1 ABSTRACT

This project addresses directly to the research need outlined in MRSON-17-01 on the topic of "Characteristics of Munitions Underwater and Their Environment". Large amount of observational and empirical data has been gathered in field and laboratory studies to reveal the mechanisms behind the motion of munitions. However, there are still knowledge gaps for the physical and deterministic explanation of the phenomenology. Our project aims to develop and utilize a three-dimensional (3D) computational model to predict the initiation of motion, continuous movement, and final deposition of munitions, which are important for site assessment and remediation actions. The 3D model captures the key physical processes which control the motion of munitions, including turbulent flow, sediment transport and scour, granular material dynamics, and the rigid-body motion of munitions. In addition, these processes are coupled and thus the developed model should be capable of simulating their interactions.

This interim report presents the current status of the project. The development of the coupled 3D model has finished. Limited validation and calibration have been performed and some preliminary results have been obtained. Several manuscripts are either under review or in preparation for journal publications. In the next phase of this project, more extensive validations and simulations will be carried out.

The developed 3D model considers the whole domain as a combination of four sub-domains, i.e., computational fluid dynamics (CFD) domain, porous bed domain, granular sediment domain (a subset of the porous bed domain), and the munition rigid body domain. Each sub-domain uses a sub-model which solves the physical processes within its boundary. The granular sediment domain and its interaction with fluids and munitions are modeled with a Smoothed Particle Hydrodynamics (SPH) model.

In the CFD domain, a 3D scour model has been developed with the use of an *immersed boundary method* (IB Method) to capture the sediment bed deformation and the possible motion of objects. Both bedload and suspended load can be simulated. The scouring of bed is solved with the Exner equation. During the development of the scour model, some new computing technologies have been proposed to deal with problems emerging from scour simulations. In particular, a slope-limited diffusive sand slide flux method is proposed to model the sliding/slumping of sediment over bed slopes which are larger than the angle of repose. Simulation results on hydrodynamics, sediment scour, and sand slide are demonstrated.

In the SPH domain, a multiphase model for both phases of water and sediment has been developed. Water is considered as a Newtonian fluid and sediment is modeled as a visco-elastoplastic material. The Drucker-Prager yield criterion is employed to determine the state of sediment material. Munitions may be mobile under the forcing from both water and sediment. The motion of munition is simulated with a 6-Degrees-of-Freedom (DoF) rigid-body motion solver. The coupling of the multiphase model and the 6-DoF rigid-body motion model has been implemented in the open-source DualSPHysics code accelerated with *graphics processing unit* (GPU) computing. Results from the model for the SPH domain and the simulated munition motion are presented.

The developed 3D model is the first of its kind which can simulate the simultaneous coupled processes of turbulent flow, sediment transport, scour, granular material dynamics, 6-DoF rigid-body motion, and ultimately the motion of munitions. With careful calibration and validation, this model adds great value to the understanding of munition dynamics in underwater environment. Specifically, this model can interrogate the munition response under different hydrodynamic forcing, sediment characteristics, munition shape, density, and initial burial.

2 OBJECTIVES

The main objective is to develop a high-fidelity computer model to predict the initiation of motion and continuous movement of munitions. To the best of our knowledge, such model does not exist before this project. The second objective is to use the developed model to simulate and analyze munition dynamics under different conditions. The comprehensive model can be used to characterize the hydrodynamic forces on underwater munitions, model sediment scour around them, and predict their mobility. Different components of the comprehensive model can be used independently to investigate a subset of physical processes. In addition, the computational modeling study compliments and benefits from other Munition Response research projects. In particular, lab and field measurements provide abundant data. However, there are important quantities for munition dynamics that are almost impossible to be measured directly. For example, the force and turning moments acting on a moving munition are extremely hard to measure. Our computer model can simulate the forces and moments at any time during munition movement. This provides critical information for the central question of munition mobility.

With the availability of such model, several hypotheses will be tested. One prevailing hypothesis regarding munition mobility is that the density of munitions controls the probability of burial or exposure. As demonstrated in the preliminary results section, the developed computer model is well suited to test this hypothesis. Another hypothesis is that the pore-pressure generation and liquefaction are among the key factors that lead to burial or exposure. Since the saturated sediment and its granular material behavior are considered in the SPH model, the simulated pore-pressure can be used for the evaluation of its importance.

Other aspects of munition dynamics which can be investigated with the computer model include:

- How do the bottom conditions (e.g., roughness, bedforms, and porosity) affect the munition stability?
- Are the empirical drag and lift coefficients accurate enough to calculate the initiation of munition motion? These coefficients have been extensively used in many simple conceptual models for munition stability.
- What are the differences between waves and current in their dislodging and transporting of munitions? Do the cyclic motion of waves and the induced rocking effect enhance munition mobility?

At the current stage, part of the above objectives have been accomplished and the rest will be done in the remaining period of the project. Specifically, we have finished the following major tasks (milestones) to achieve the above objectives:

- the CFD model using IB method for turbulent flow, the key driving force for munition movement, has been validated and compared with experimental data.
- the 3D model for scour around objects has been developed. The object can be either fixed or mobile. A new physically-based sand slide method is proposed in the scour model by solving a slope-limited diffusion equation.
- the SPH multiphase model has been developed to capture the granular sediment behavior and its interaction with the munition.
- the coupling of SPH multiphase model with the 6-DoF rigid-body motion model has been completed. Validations have been carried out to compare the simulation results with laboratory experiment on a specially designed and well instrumented penetrometer (in collaboration with Dr. Nina Stark at Virginia Tech). More calibration and validation will be performed.

3 TECHNICAL SECTION

3.1 The structure of the modeling framework

The computational framework is designed to predict the initiation of motion and continuous movement of munitions. In order to achieve this, the physically-based model needs to include all the processes in the system. The most important physical processes contributing to the fate of underwater munitions include turbulent flow field and its induced sediment transport, hydrodynamic forces on the munitions and their 6-DoF motion, pore pressure generation and possible liquefaction within the underlying bed, as well as the behavior of the granular bed supporting the munitions (see Figure 1).

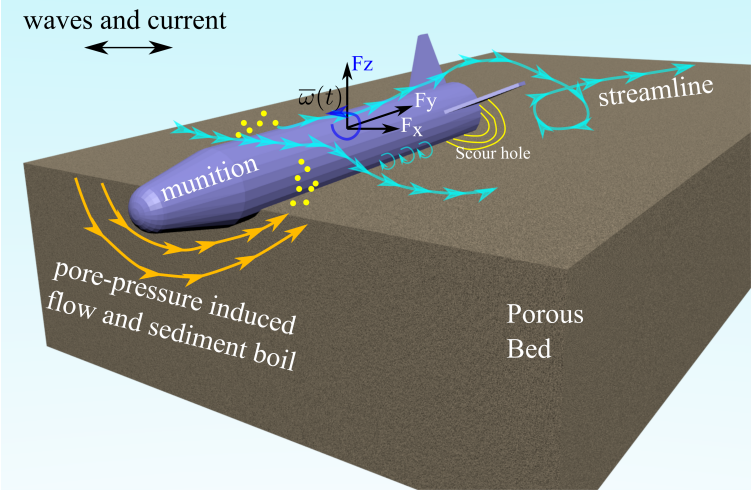

Figure 1: Physical processes governing the munition dynamics.

Corresponding to the identified key physical processes, the comprehensive modeling framework decomposes the simulation domain into several sub-domains as shown in Figure 2. This is probably the most convenient and natural way to deal with the complexity and multi-physics nature of the problem. In general, each sub-domain deals with one major physical processes and the coupling between each sub-domain pair is through their common boundaries. There are four sub-domains:

- CFD flow domain: Turbulent flow field and suspended sediment transport are simulated within this domain. At the interface with the bed, bedload transport flux is calculated with the simulated wall shear stress. To track the deforming bed due to scour, an immersed boundary method is used to implicitly represent the bottom of the flow domain. In an immersed boundary method, a wall is not explicitly represented by the computational mesh. Instead, its effect to flow is implicitly modeled. An immersed boundary method can easily deal with large deformation and displacement. The munitions are also represented by the immersed boundary method because of their movement and interactions with the bed. The flow and sediment transport solver has been implemented in the open source CFD package OpenFOAM (OpenCFD, 2019).
- SPH granular sediment domain: This is a sub-domain within the porous bed underneath the munition (see Figure 2). This part is a subset of the porous bed domain. A Smoothed Particle Hydrodynamics (SPH) method is used to model the granular sediment behavior and its interaction with munitions. The open source code *DualSPHysics* accelerated with GPU computing is used (Crespo et al., 2015). New development for the purpose of this project includes the addition of the SPH multi-phase model and the 6-DoF rigid-body motion solver.

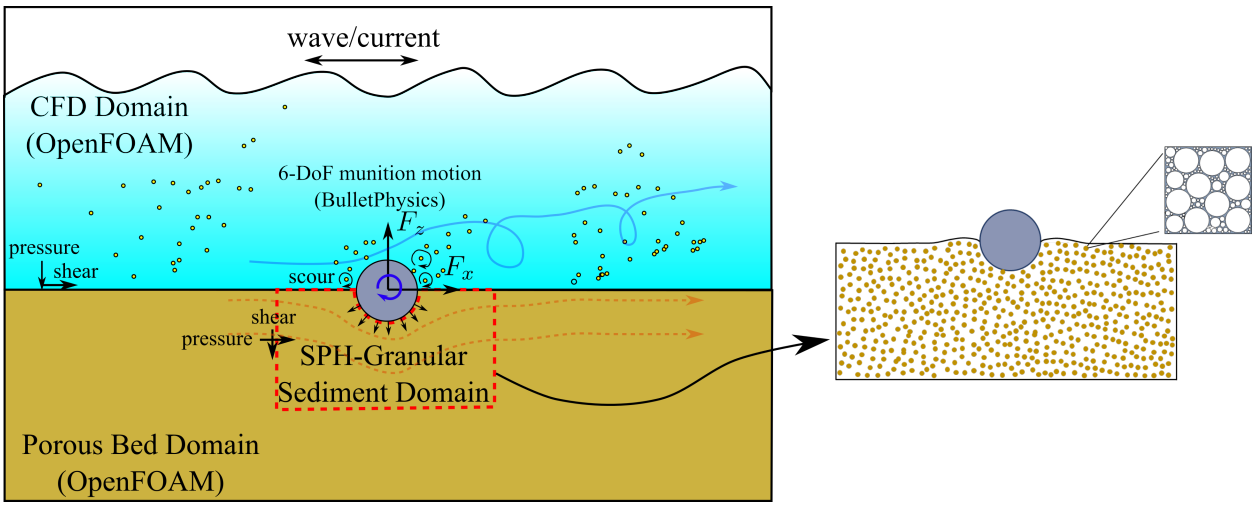

Figure 2: Composition and structure of the integrated computational model. The coupling and embedment of different model domains are also shown.

- Porous bed domain: The bed is made of loose sediment and thus it can be treated with classic porous media flow theory. The flow within the bed is mainly driven by the uneven pressure distribution induced by turbulence and the presence of munition. Theoretically, the pressure of pore-water can be modeled with poro-elastic or poro-elasto-plastic soil models. During this project, and more importantly for the purpose of munition motion prediction, it is decided that this part is redundant to the SPH granular sediment domain model described above. Indeed, the SPH model for sediment, though in a reduced size domain, uses a poro-elasto-plastic soil model. The porous bed response has already been modeled with the SPH code.
- Munition 6-DoF motion domain: This domain is the rigid body of the munition itself. With the hydrodynamics forces and the granular material forces (from the SPH model), the 6-DoF rigid-body motion model has been implemented in the open-source *DualSPHysics* code.

With the introduction of the physical processes and corresponding sub-domains, the details of the mathematical models and their implementations are described next. During the development of such a complex coupled modeling system, innovative ideas and solutions are invented and adopted to solve some newly discovered technical difficulties. For example, within the scour hole around the munitions, there will be places where the local bed angle exceeding the angle of repose. Under gravity, sediment will slide down the slope until the bed angle is less than the angle of repose. Although has been studied in the literature, this sand slide process is hard to model because its physics is not included in the sediment transport theory. To deal with that, a new diffusive-flux based method is proposed.

3.2 Technical Approach

3.2.1 CFD flow domain

Turbulent flow field and sediment transport are solved in this domain. Turbulent field adjacent to objects depends on many factors, such as shape and size of objects, bedform and bed material. To capture more details of the flow field, a 3D *computational fluid dynamics* (CFD) model is applied to solve the Reynolds-Averaged Navier-Stokes (RANS) equations. The flow in this problem can be considered as incompressible, viscous, and Newtonian. When the flow field (velocity, turbulence, and wall shear stress) is known, it will

be used to solve for the sediment transport. On the other hand, the sediment mass conservation equation, namely the Exner equation, is solved once the sediment fluxes are available. Because the morphological time scale is much larger than the flow time scale, the bed elevation is not updated in every flow time step. If such approach is not used, the computational cost will be unnecessarily high.

Flow models: To solve the turbulent flow field, the Reynolds-averaged Navier-Stokes equations can be written as:

$$\text{Continuity equation: } \nabla \cdot \overline{\mathbf{u}} = 0 \tag{1}$$

$$\text{Momentum equation: } \frac{\partial \overline{\mathbf{u}}}{\partial t} + \nabla \cdot (\overline{\mathbf{u}}\overline{\mathbf{u}}) = -\nabla \overline{p} + \nu \nabla^2 \overline{\mathbf{u}} - \nabla \cdot \boldsymbol{\tau} \tag{2}$$

where $\overline{\mathbf{u}}(\overline{u}, \overline{v}, \overline{w})$ is flow velocity, $\overline{p}$ is pressure divided by fluid density, ν is molecular viscosity, and $\boldsymbol{\tau}$ is the Reynolds stress, which is closed by turbulence models. The computational platform adopted in this work is OpenFOAM, which provides a rich selection of turbulence models. The CFD solver, *pimpleFoam* in OpenFOAM is modified to have immersed boundary method capability. As a result, the turbulence models also need to be modified. Within the scope of this project, only one RANS model is used and will be described below.

According to the Boussinesq approximation, the Reynolds stresses $\boldsymbol{\tau}$ can be expressed as the product of eddy viscosity and the mean strain rate:

$$\boldsymbol{\tau} = -\nu_t \frac{1}{2} \left(\nabla \overline{\mathbf{u}} + (\nabla \overline{\mathbf{u}})^T \right) + \frac{2}{3} k \mathbf{I} \tag{3}$$

where ν_t denotes the eddy viscosity and k is the turbulence kinetic energy.

Here, a widely used RANS model, i.e., the standard $k - \omega$ model is introduced as an example (Wilcox, 2006). The other popular RANS model, the $k - \epsilon$ model was also used in this work. ω is the specific dissipation rate. The transport equations for k and ω are:

$$\frac{\partial k}{\partial t} + \overline{\mathbf{u}} \cdot (\nabla k) = \boldsymbol{\tau} : (\nabla \overline{\mathbf{u}}) - \beta^* k \omega + \nabla \cdot \left[(\nu + \sigma^* \nu_t) \nabla k \right] \tag{4}$$

$$\frac{\partial \omega}{\partial t} + \overline{\mathbf{u}} \cdot (\nabla \omega) = \alpha \frac{\omega}{k} \boldsymbol{\tau} : (\nabla \overline{\mathbf{u}}) - \beta \omega^2 + \nabla \cdot \left[(\nu + \sigma \nu_t) \nabla \omega \right] \tag{5}$$

where $\alpha = 5/9$, $\beta = 3/40$, $\beta^* = 9/100$, and σ=$\sigma^* = 1/2$.

Sediment transport model: Sediment transport induced by the turbulent flow is divided into bed-load and suspended load transport. Suspended sediment denotes the bed particles transported by turbulence in the water column and is simulated within this CFD domain by solving an advection-diffusion equation in the form of

$$\frac{\partial \overline{C}}{\partial t} + \overline{\mathbf{u}} \frac{\partial \overline{C}}{\partial x} + \overline{\mathbf{u}} \frac{\partial \overline{C}}{\partial x} + (\overline{w} - v_s) \frac{\partial \overline{C}}{\partial z} = \nabla [D_d \nabla \overline{C}] \tag{6}$$

where $\overline{C}$ is volumetric suspended sediment concentration averaged over turbulence, v_s is the sediment settling velocity, and D_d denotes the kinematic eddy diffusivity of suspended sediment.

The deposition rate D near the bed under non-equilibrium condition can be evaluated as

$$D = v_s \overline{C}_b \tag{7}$$

where $\overline{C}_b$ is the sediment concentration near the bed ($z = b$) and b is a reference height. The entrainment rate E near the bed is calculated as

$$E = v_s \tilde{E} \tag{8}$$

where $\tilde{E}$ is the dimensionless entrainment rate and equal to the near-bed concentration under equilibrium condition (van Rijn, 1984). This rate in equilibrium condition can be calculated by one of the entrainment laws in sediment transport theory.

At the interface of turbulent flow with the porous bed, bedload transport rate represents the movement of particles along the bed. It can be estimated as a function of wall shear stress on bed. Here, the empirical formula proposed in Engelund and Fredsøe (1976) is adopted:

$$q^* = \begin{cases} 18.74(\theta - \theta_c)(\theta^{1/2} - 0.70\theta_c^{1/2}) & \text{if } \theta > \theta_c \\ 0 & \text{otherwise} \end{cases} \tag{9}$$

where q^* denotes the dimensionless bed-load transport rate defined as

$$q^* = \frac{q_0}{\sqrt{Rgd}d} \tag{10}$$

where q_0 is bedload transport rate for flat horizontal bed; θ and θ_c are the Shields number and critical Shields number, respectively. θ is given as:

$$\theta = \frac{\tau_b}{\rho g R d} \tag{11}$$

where τ_b is the wall shear stress on bed calculated from hydrodynamic model, $R = 1.65$ for quartz, and d is grain size.

To model the effect of local bed slope and local flow direction, θ_c is adjusted according to (Engelund and Fredsøe, 1976):

$$\theta_c = \theta_{c0}(\cos\beta_1 \sqrt{1 - \frac{\sin^2\beta_2 \tan^2\beta_1}{\mu_s^2}} - \frac{\cos\beta_2 \sin\beta_1}{\mu_s}) \tag{12}$$

where β_1 is the angle of local bed, β_2 is the angle between local flow velocity and bed slope, and μ_s is the static friction coefficient. The critical Shields number on a flat horizontal bed θ_{c0} is calculated from the empirical formula amended by Parker et al. (2003).

Bedload transport rate $\mathbf{q}_b$ also needs to be corrected according to the bed slope as

$$\mathbf{q}_b = q_0 \frac{\boldsymbol{\tau}_b}{|\boldsymbol{\tau}_b|} - C|q_0|\nabla z_b \tag{13}$$

where z_b is the bed elevation and C is an empirical constant adopted to control the additional sediment flux by bed slope (Brørs, 1999).

With the availability of suspended load and bedload fluxes, the Exner equation is solved to update the bed elevation based on the continuity of sediment as

$$\frac{\partial z_b}{\partial t} = \frac{1}{1-n}(-\nabla \cdot \mathbf{q}_b + D - E) \tag{14}$$

where n is bed porosity.

Three-dimensional scour modeling is not trivial and involves many other details. One of the difficulties that we have to deal with in the model development phase is the sand slide algorithm (Figure 3). It has been researched in the literature. However, all previous algorithms are either not stable or specifically

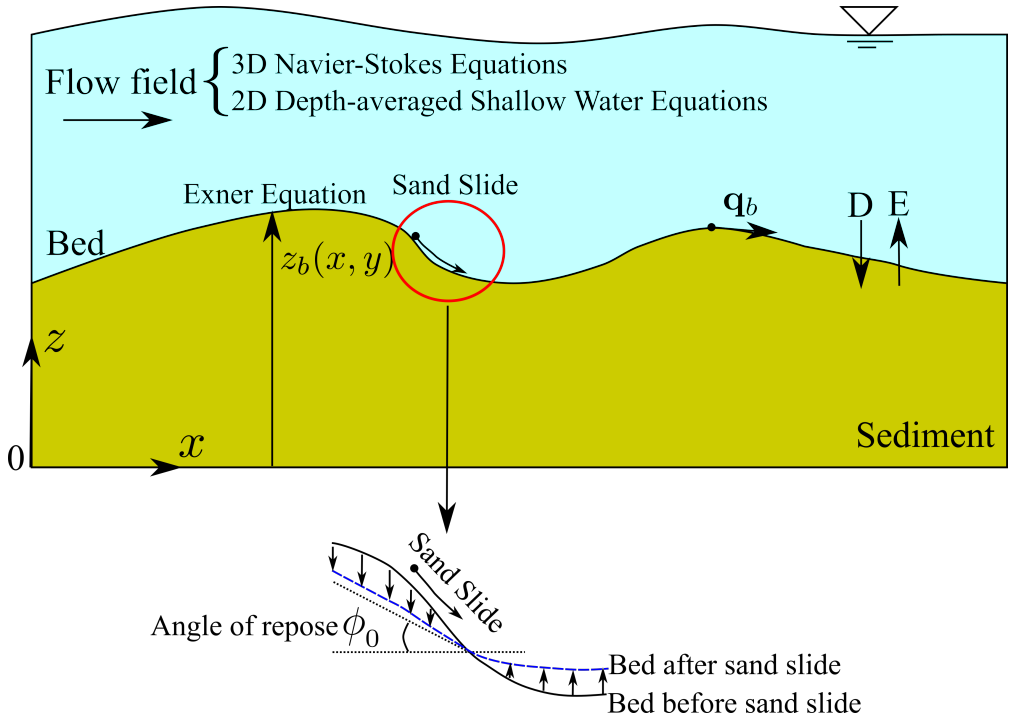

Figure 3: The sand slide process in scour hole.

designed for one scour code. We found they did not fit well into our scour model. Thus, a new algorithm was developed.

In the process of sediment transport, sand slide happens when local bed slope exceeds the angle of repose ϕ_0 (Figure 3). Sand slide will continue until the bed slope is equal to or below the angle of repose. In other words, sand will move from high elevation to low elevation to reduce the bed angle. It is similar to the diffusion process or heat transfer process. However, one major difference is the in heat transfer, the final status is a uniform temperature while in sand slide the equilibrium is reached once the bed slope is in compliance. Based on this observation, we propose a slope-limited diffusion equation to simulate the sand slide process. In addition, special treatment is developed such that this method is computationally efficient and independent of bed mesh type, which will be shown in the next section.

Similar to Fick's law of diffusion, the diffusive sand slide flux can be written as

$$\mathbf{q} = -K\nabla z_b \tag{15}$$

where $\mathbf{q}$ is the sand slide flux and K is the sand slide diffusivity (L^2/T).

In the context of sand slide, one deviation from the Fick's law is that the flux is limited by the bed slope. If the bed angle is less than or equal to the angle of repose, there is no sand slide and thus the flux should be zero. Therefore, the flux formula in Eq. 15 should be limited by the bed slope. To achieve this, the diffusivity K should be a conditional function as follows:

$$K = \begin{cases} K_0, & \text{if } |\nabla z_b| \geq \tan\phi_0 \\ 0, & \text{otherwise} \end{cases} \tag{16}$$

where K_0 is the diffusivity once sand slide initiates and has a constant value in this work.

Combined with the mass balance of sliding sand, the governing equation for bed elevation is then

$$\frac{\partial z_b}{\partial t} = K\nabla^2 z_b \tag{17}$$

This unsteady, slope-limited diffusion equation can be easily solved to update the bed elevation z_b such that bed slope everywhere is in compliance.

Immersed boundary method: One key component of the scour model for this project is the adopted immersed boundary method. Traditional Arbitrary-Lagrangian-Eulerian (ALE) mesh deformation method cannot deal with large scour holes and complex geometries, e.g., munition with fins. In the IB method, simulations are carried out on a simple Cartesian grid (Figure 4) and the boundary condition of moving bed is imposed implicitly by fixing velocity of the IB cells (the volume fraction of sediment between "0" and "1" in Figure 4) in the RANS equations. Comparing to the ALE method, the immersed boundary method has great flexibility to deal with very complex and evolving scour-hole geometries.

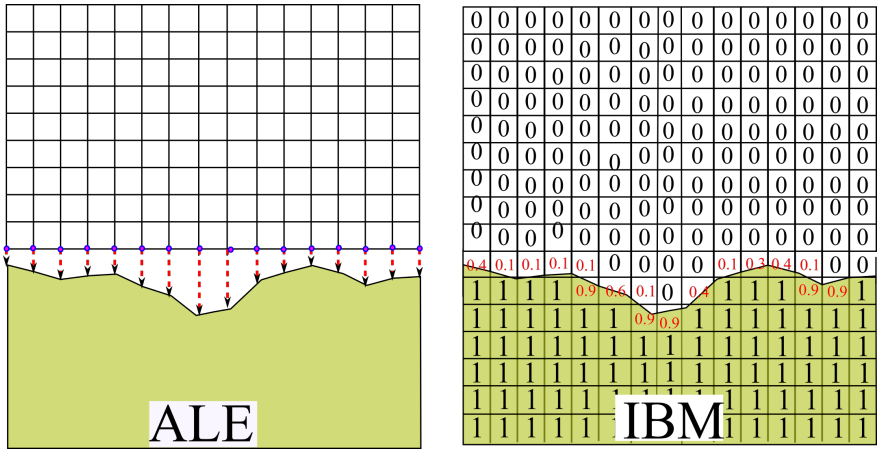

Figure 4: Arbitrary-Lagrangian-Eulerian (ALE) vs. immersed boundary method (IBM) for the tracking of scoured bed.

Similar to other IB methods in the literature (Gilmanov and Sotiropoulos, 2005; Jasak et al., 2014; Jasak and Tuković, 2015; Gilmanov et al., 2015), the present method classifies the cells in a computational domain into three categories: IB cells, live cells, and dead cells (see Figure 5). IB cells are the cells closest to the immersed surface Γ_{IB} in the fluid region. They are used to impose conditions on immersed boundaries. The algorithm to determine the flags of IB, live and dead cells is as follows:

Step 1: find all the cells intersecting with immersed surface Γ_{IB},

Step 2: label the cells, excluding the intersecting cells, in fluid and solid regions as live an dead cells, respectively,

Step 3: for each intersecting cell:

- if the cell center is in the fluid region, it is labeled as IB cell;
- otherwise, it is labeled as dead cell, and re-label its adjacent live cells (sharing a boundary) as IB cells.

For each IB cell, a "hit point" (black dot in Figure 5) is then calculated as the normal projection of the IB cell center (black cross in Figure 5) to the immersed boundary. An "image point" (black circle in Figure 5) is

the image of a hit point with respect to the IB cell center. These different points are used in the calculation of immersed boundary method.

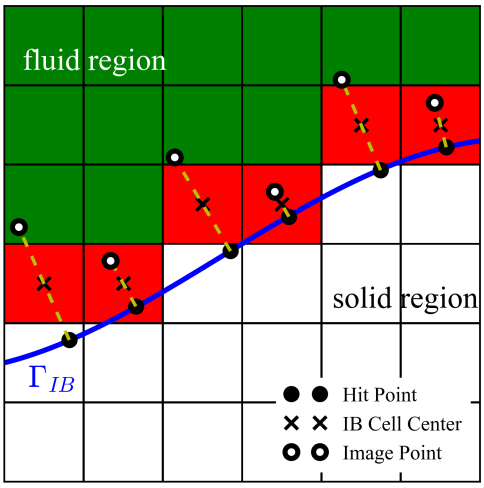

Figure 5: Schematic view of IB representation: IB cell centers (black cross), hit points (black dots), image points (black circles), IB cells (red filled), live cells (green filled), and dead cells (white filled). Immersed interface Γ_{IB} is represented by the blue curve.

To enforce the correct flow behavior near an immersed boundary Γ_{IB}, flow variables at IB cell centers are reconstructed based on their required boundary conditions. The reconstruction requires a proper interpolation stencil which depends on specific interpolation scheme. In this work, the interpolation stencil only contains live and IB cells and the building process of interpolation stencil is as follows:

Step 1: find the cell that contains the image point, namely image cell. If image point is located in dead cells or outside of the computational domain, find the nearest IB/live cell as its image cell.

Step 2: search and select the neighbouring live and IB cells which share face with this image cell. These neighbouring cells are named as the first-row cells.

Step 3: search and select the neighbouring live and IB cells of the first-row cells. These neighbouring cells are named as the second-row cells, which should exclude those already in the first-row cell list.

Step 4: repeat Step 2 until the total number of the neighbouring cells for each IB cell is larger than a specified value, which may depend on the interpolation scheme.

Step 5: sort all the neighbouring cells based on the distance to image point.

The interpolation stencil searching algorithm as well as the interpolation scheme may be very expensive if the stencil is too large. It is more efficient and cheaper to use image point, instead of IB cell center, as the center of the interpolation stencil. In parallel computation, if cells in the interpolation stencil are located in other processors, it will incur additional communication cost.

As suggested in Mittal and Iaccarino (2005), higher-order interpolation needs to be used for high Reynolds number problems. In this work, a second-order (quadratic) polynomial interpolation scheme is implemented as follows (Seo and Mittal, 2011; Jasak et al., 2014; Jasak and Tuković, 2015; Singh et al., 2015):

$$\tilde{\phi}(\tilde{x},\tilde{y},\tilde{z}) = \sum_{i=0}^{2}\sum_{j=0}^{2}\sum_{k=0}^{2} C_{ijk}\tilde{x}^i\tilde{y}^j\tilde{z}^k, \quad i+j+k \leqslant 2 \tag{18}$$

where $\tilde{x} = x - x_{\mathrm{HP}}$, $\tilde{y} = y - y_{\mathrm{HP}}$, and $\tilde{z} = z - z_{\mathrm{HP}}$ are local (relative) coordinates of a stencil cell center (x, y, z). Subscript HP denotes hit point. $\tilde{\phi}(\tilde{x},\tilde{y},\tilde{z})$ is a polynomial function to approximate $\phi(x, y, z)$, a generic flow variable at (x, y, z). Considering the restriction on i, j, and k, this polynomial has 10 unknown coefficients C_{ijk} in total. For a given IB cell, it is assumed that there are M cells in its interpolation stencil. For this selected stencil, Eq. (18) can be written in the form of matrix-vector product

$$\boldsymbol{\phi} = \mathbf{A}\boldsymbol{c} \tag{19}$$

where $\boldsymbol{\phi}$ denotes a vector of size M. $\boldsymbol{c}$ denotes a vector consisting of the 10 unknown coefficients C_{ijk}. $\mathbf{A}$ denotes a $M \times 10$ matrix, which can be computed by the local coordinates of each stencil cell center. A weighted least squares approach is adopted to determine the unknown coefficients (Li, 1998; Seo and Mittal, 2011). For each cell in the interpolation stencil, the weight function w_0 can be written as

$$w_0 = \frac{1}{2}\left[1 + \cos\left(\frac{\delta}{1.1\delta_{max}}\pi\right)\right] \tag{20}$$

where δ is the distance between a stencil cell center and the corresponding hit point. δ_{max} is the maximum value of δ. Applying the weight function to both sides of Eq. (19) and solving for $\boldsymbol{c}$, one can get

$$\mathbf{W}\boldsymbol{\phi} = \mathbf{W}\mathbf{A}\boldsymbol{c} \tag{21}$$

$$\boldsymbol{c} = (\mathbf{W}\mathbf{A})^{-1}\mathbf{W}\boldsymbol{\phi} \tag{22}$$

where $\mathbf{W}$ is a $M \times M$ matrix with w in Eq. (20) as its elements. This weighted least squares technique has been proven to have the advantages of robustness, smooth error distribution and locally-supported second-order accuracy (Li, 1998).

Dirichlet and Neumann boundary conditions are typical for flow variables on immersed boundary. A generic quadratic function for the Dirichlet boundary condition can be derived from Eq. (18) as follows

$$\tilde{\phi}(\tilde{x},\tilde{y},\tilde{z}) = \phi_{\mathrm{HP}} + \sum_{i=0}^{2}\sum_{j=0}^{2}\sum_{k=0}^{2} C_{ijk}\tilde{x}^i\tilde{y}^j\tilde{z}^k, \quad 0 < i+j+k \leqslant 2 \tag{23}$$

where the number of unknown coefficients C_{ijk} is reduced to 9. $\mathbf{A}$ then becomes a $M \times 9$ matrix, and the vector $\boldsymbol{c}$ has a length of 9:

$$\mathbf{A} = \begin{bmatrix} x_1 & y_1 & z_1 & x_1y_1 & x_1z_1 & y_1z_1 & x_1^2 & y_1^2 & z_1^2 \\ x_2 & y_2 & z_2 & x_2y_2 & x_2z_2 & y_2z_2 & x_2^2 & y_2^2 & z_2^2 \\ & & & & \vdots & & & & \\ x_M & y_M & z_M & x_My_M & x_Mz_M & y_Mz_M & x_M^2 & y_M^2 & z_M^2 \end{bmatrix}, \quad \boldsymbol{c} = \begin{bmatrix} c_{100} \\ c_{010} \\ \vdots \\ c_{002} \end{bmatrix} \tag{24}$$

Similarly, for the Neumann boundary condition with zero gradient on the immersed boundary, the mathematical formula can be written as

$$\nabla\phi_{\mathrm{HP}} \cdot \mathbf{n}_{\mathrm{HP}} = 0 \tag{25}$$

where $\mathbf{n}_{HP}$ is the normal direction to the immersed boundary Γ_{IB} at the hit point. The number of unknown coefficients is 10 and the matrix system becomes:

$$\mathbf{A} = \begin{bmatrix} 1 & x_1 & y_1 & z_1 & x_1y_1 & x_1z_1 & y_1z_1 & x_1^2 & y_1^2 & z_1^2 \\ 1 & x_2 & y_2 & z_2 & x_2y_2 & x_2z_2 & y_2z_2 & x_2^2 & y_2^2 & z_2^2 \\ & & & & \vdots & & & & & \\ 1 & x_M & y_M & z_M & x_My_M & x_Mz_M & y_Mz_M & x_M^2 & y_M^2 & z_M^2 \\ 0 & n_{\mathrm{HP},x} & n_{\mathrm{HP},y} & n_{\mathrm{HP},z} & 0 & 0 & 0 & 0 & 0 & 0 \end{bmatrix}, \quad \boldsymbol{c} = \begin{bmatrix} c_{000} \\ c_{100} \\ c_{010} \\ \vdots \\ c_{002} \end{bmatrix} \tag{26}$$

where $n_{\mathrm{HP},x}$, $n_{\mathrm{HP},y}$, $n_{\mathrm{HP},z}$ denote the x, y, z components of wall normal vector $\mathbf{n}_{\mathrm{HP}}$. $\mathbf{A}$ becomes a $(M+1)\times(M+1)$ matrix. The extra row in Eq. (26) is obtained by incorporating boundary condition in Eq. (25) into Eq. (19). Once the matrix systems are constructed, the coefficients C_{ijk} for Dirichlet and Neumann boundary conditions can be obtained by solving Eqs. (24) and (26).

The IB wall function in this work is based on the two-layer wall model proposed in Roman et al. (2009). One of the key parameters in a wall model for wall-bounded turbulent flow is the shear velocity u_τ. Here, the shear velocity is calculated with the flow information at image point, which is more representative than the constructed values in IB cell. Usually, it is assumed that local equilibrium exists in the near wall region flow, meaning $P_k \approx \epsilon$ at image point. Thus, for a given IB cell and its corresponding image point, u_τ can be estimated as $C_\mu^{1/4}\sqrt{k_{\mathrm{IP}}}$, and the dimensionless wall distance $y^+ = u_\tau y/\nu$ is calculated as

$$y_{\mathrm{IP}}^+ = \frac{C_\mu^{1/4}\sqrt{k_{\mathrm{IP}}}\,y_{\mathrm{IP}}}{\nu}, \quad y_{\mathrm{IB}}^+ = y_{\mathrm{IP}}^+\frac{y_{\mathrm{IB}}}{y_{\mathrm{IP}}} \tag{27}$$

where y_{IP} denotes the distance from image point to immersed boundary, y_{IB} denotes the distance from IB cell center to immersed boundary. The ratio of $y_{\mathrm{IP}}/y_{\mathrm{IB}}$ is set to be 2 in this work.

According to the two-layer wall model, the shear velocity can be calculated as

$$u_\tau = \begin{cases} C_\mu^{1/4}\sqrt{k_{\mathrm{IP}}} & \text{if } y_{\mathrm{IP}}^+ > y_{\mathrm{Laminar}}^+ \\ \sqrt{\nu|u_{\mathrm{tan,IP}}^{old}|/y_{\mathrm{IP}}} & \text{if } y_{\mathrm{IP}}^+ \leqslant y_{\mathrm{Laminar}}^+ \end{cases} \tag{28}$$

where $u_{\mathrm{tan,IP}}^{old}$ denotes the interpolated tangential velocity at image point from previous time step or iteration, and $|\,|$ denotes its magnitude. The threshold y_{Laminar}^+ has a value of 11. With the shear velocity, the wall shear stress can be calculated as

$$\tau_w = \rho u_\tau^2 \tag{29}$$

For the two points (image point and IB cell center) along the same line perpendicular to the immersed boundary, their velocity should follow the same log-law, i.e., with the same shear velocity. Therefore, the tangential velocity at IB cell center can be calculated as

$$u_{\mathrm{tan,IB}}^{\mathrm{new}} = \begin{cases} \dfrac{u_\tau\kappa}{\log(Ey_{\mathrm{IB}}^+)} & \text{if } y_{\mathrm{IB}}^+ > y_{\mathrm{Laminar}}^+ \\ u_\tau y_{\mathrm{IB}}^+ & \text{if } y_{\mathrm{IB}}^+ \leqslant y_{\mathrm{Laminar}}^+ \end{cases} \tag{30}$$

where E is an empirical coefficient with a value of 9.8 for smooth walls. Following this, the new values of eddy viscosity ν_t, k, and ϵ at IB cell center can be calculated as

$$\nu_t = \begin{cases} \dfrac{y_{\mathrm{IB}}^+\kappa}{\log(Ey_{\mathrm{IB}}^+)}\nu & \text{if } y_{\mathrm{IB}}^+ > y_{\mathrm{Laminar}}^+ \\ 0 & \text{if } y_{\mathrm{IB}}^+ \leqslant y_{\mathrm{Laminar}}^+ \end{cases} \tag{31}$$

$$k_{\mathrm{IB}}^{\mathrm{new}} = \begin{cases} (\nu_t + \nu)\dfrac{u_{\mathrm{tan,IP}}^{\mathrm{old}}}{y_{\mathrm{IP}}} C_\mu^{-0.5} & \text{if } y_{\mathrm{IB}}^+ > y_{\mathrm{Laminar}}^+ \\ k_{\mathrm{IP}} & \text{if } y_{\mathrm{IB}}^+ \leqslant y_{\mathrm{Laminar}}^+ \end{cases} \tag{32}$$

$$\epsilon_{\mathrm{IB}}^{\mathrm{new}} = \begin{cases} \dfrac{C_\mu^{0.75}(k_{\mathrm{IB}}^{\mathrm{new}})^{1.5}}{\kappa y_{\mathrm{IB}}} & \text{if } y_{\mathrm{IB}}^+ > y_{\mathrm{Laminar}}^+ \\ \epsilon_{\mathrm{IP}} & \text{if } y_{\mathrm{IB}}^+ \leqslant y_{\mathrm{Laminar}}^+ \end{cases} \tag{33}$$

Many applications in natural and built environments involve the flow and transport over rough boundaries, for example the river bed and ocean floor where sediment transport occurs. To cope with that, the present wall function for immersed boundary method is also designed to include the roughness effect. The rough wall function changes the value of coefficient E as a function of a non-dimensional roughness height k_s^+. The functional form of the empirical formula is

$$E = \begin{cases} 0.9\left(\dfrac{k_s^+ - 2.25}{87.75} + 0.5k_s^+\right)^{-\sin\left[0.4258\left(\log k_s^+\right) - 0.811\right]} & \text{if } k_s^+ > 90 \\ 0.9\left(1 + 0.5k_s^+\right)^{-1} & \text{if } k_s^+ \leqslant 90 \end{cases} \tag{34}$$

where $k_s^+ = u_\tau k_s/\nu$.

The wall function in the immersed boundary method described above, similar to almost all wall functions developed with immersed boundary method, often produces non-smooth wall shear stress distribution. In many applications such as sediment transport and erosion where the flux depends on the wall shear, the smoothness of wall shear is of critical importance. In this section, the original wall function and its ill behavior when used with immersed boundary method are firstly analyzed. Then, a new y^+-adaptation method is proposed. For easy argument, Figure 6a shows a schematic view of 1D boundary layer flow near an immersed boundary. It defines wall distances, y_{IB} and y_{IP}, which are the wall distance from IB cell center and image point, respectively. The location of immersed boundary Γ_{IB} can be varied to change the wall distances y_{IB} and y_{IP}.

For many wall functions used with RANS models, it is often required that the near-wall cell center is in the log-law layer, i.e., the non-dimensional wall distance y^+ is larger than 30. However, this requirement may not always be satisfied in IB method. The reason is that the background grid is fixed and the immersed boundary geometry is arbitrary. As a result, there is no direct control on the wall distances y_{IB} and y_{IP}. In addition, the immersed boundary may move and consequently wall distances may dynamically change. It is likely very small wall distances will result and thus violate the y^+ requirement for wall functions. When the wall distances are small, i.e., the IB cell and IP point are within the viscous or buffer layer, the resulted wall shear is very different. The cause of this difference is that the wall function stipulates a nonlinear and discontinuous behavior depending on whether y_{IB}^+ is larger or smaller than y_{Laminar}^+.

To prove this point, a simple 1D turbulent channel flow with $Re = UH/\nu = 5 \times 10^5$ is simulated using the setup in Figure 6a where the immersed boundary can be shifted vertically to vary the wall distance. Here, the mean velocity U = 0.5 m/s, the channel depth H = 1 m, and the kinematic viscosity $\nu = 10^{-6}$ m^2/s. The boundary is smooth. Assuming a fully developed open channel flow, the calculated theoretical shear velocity is 1.84 cm/s. The simulated shear velocity and corresponding IB cell wall distance are plotted in Figure 6b. It is observed that when the IB cell center is in the log-law layer, i.e., $y_{\mathrm{IB}}^+ > 30$, the simulated shear velocity approaches the theoretical value. However, when the IB cell is located closer to the immersed

boundary and not in the log-law layer, the simulated shear velocity has significant error and the error increases when the wall distance decreases.

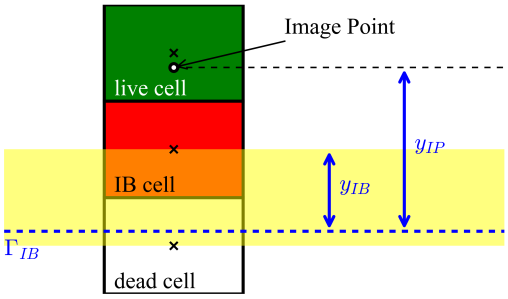

(a) 1D schematic view of wall distances from IB cell center and image point

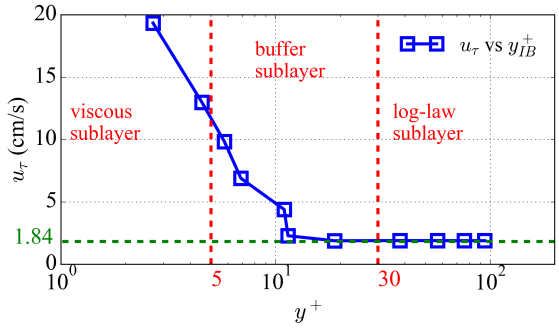

(b) Simulated shear velocity as a function of y^+_{IB}

Figure 6: Effect of IB cell wall distance on the simulated shear velocity. y^+_{IB} and y^+_{IP} denote the dimensionless wall distance of IB cell center and image point, respectively. The immersed boundary Γ_{IB} can be moved vertically in the yellow region to change the IB cell wall distance.

The root of the ill behavior of wall shear is the lack of control on wall distance in immersed boundary method. To overcome this problem, a y^+-adaptation algorithm is developed. The basic idea is to adjust the IB cells if their wall distance is too small. Specifically, if $y^+_{\mathrm{IP}} < 30$ or $y^+_{\mathrm{IB}} < 11$, the corresponding IB cell will be set as dead cell and a new IB cell will be searched for among its neighbouring live cells in the direction away from the immersed boundary (see Figure 7a). At every time step, this adaptation of IB cell will continue until all IB cells are located in the log-law layer. Figure 7b shows the same 1D channel flow case with the adaptation treatment. It is found that regardless the initial IB cell wall distance, the algorithm automatically adjusts and makes sure that the IB cell is located in the log-law layer ($y^+_{\mathrm{IB}} > 11$ and $y^+_{\mathrm{IP}} > 30$). In addition, the resulted shear velocity is almost constant ($\approx$1.8 cm/s) for any given initial IB cell wall distance.

It is noted that the adaptation ensures well-behaved wall shear stress with the cost of slight reduction in how accurately the immersed boundary is represented by the labeling of IB, fluid, and dead cells. However, this reduction in accuracy is not significant if mesh is sufficiently refined near the immersed boundary.

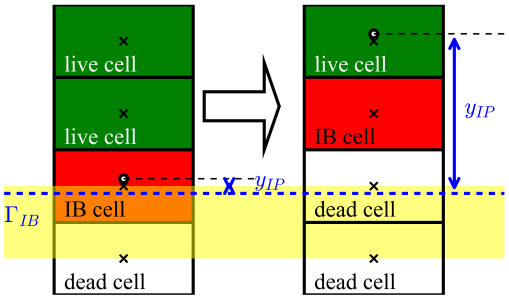

(a) 1D schematic of the y^+ adaptation process

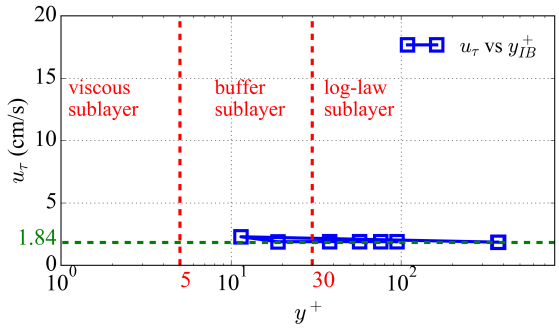

(b) after y^+ adaptation

Figure 7: Effect of IB y^+ adaptation on calculated shear velocity.

3.2.2 Porous bed and SPH granular sediment domain

The sediment bed domain is treated as a two-phase material which consists of fluid and sediment particles. Before the mathematical formulations for the two-phase bed model are presented, the basic idea of the SPH method is presented.

SPH method: In the SPH method, the computational domain is discretized with a finite number of particles, which is shown using a 2D example in Figure 8. These particles can carry material properties such as density, mass, stress etc., which move with the material velocity. The material properties of each particle are calculated through the use of summation process over its neighboring particles with a kernel function. Integral representation of a field function $f(\mathbf{x})$ can be written as:

$$\langle f(\mathbf{x})\rangle = \int_\Omega f(\mathbf{x}')W(\mathbf{x}-\mathbf{x}',h)d\mathbf{x}' \tag{35}$$

where $W(\mathbf{x}-\mathbf{x}',h)$ is the kernel function, and h is the smoothing length which defines the influence domain of W. The smoothing function $W(\mathbf{x}-\mathbf{x}',h)$ should satisfy several conditions. The first one is the normalization condition which has the form of

$$\int_\Omega W(\mathbf{x}-\mathbf{x}',h)d\mathbf{x}' = 1 \tag{36}$$

The second condition is that when the smoothing length approaches zero, the smoothing function should approach the delta function:

$$\lim_{h\to 0} W(\mathbf{x}-\mathbf{x}',h) = \delta(\mathbf{x}-\mathbf{x}') \tag{37}$$

The third is the compact support condition:

$$W(\mathbf{x}-\mathbf{x}',h)=0 \qquad \text{when } |\mathbf{x}-\mathbf{x}'|>\kappa h \tag{38}$$

where κ is a constant which controls the effective area of the smoothing function.

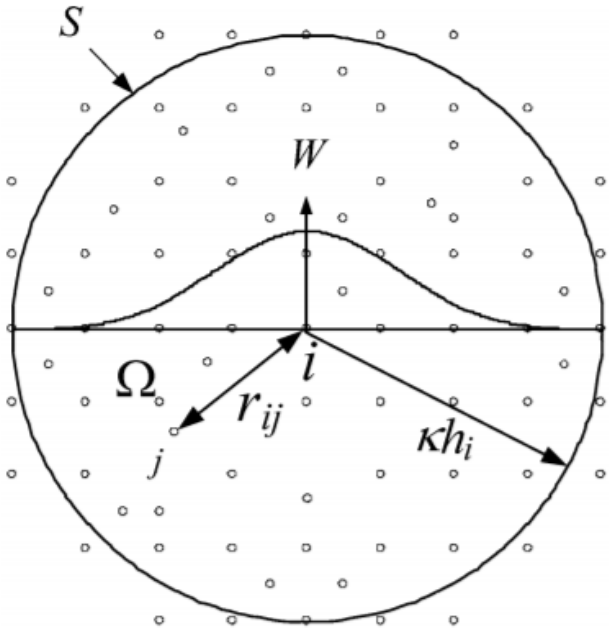

Figure 8: Particle approximation in SPH method (Liu and Liu, 2010).

With the above definitions in the SPH method, the governing equations can be descretized. The Lagrangian form of the Navier-Stokes equations are discretized using the SPH scheme to approximate the multiphase flows in this work. Greek superscripts α and β denote coordinate directions. In the following, the notation of Einstein's summation is used. The continuity and momentum equations in the Lagrangian form can be written as

$$\frac{d\rho}{dt}+\rho\frac{\partial u^{\alpha}}{\partial x^{\alpha}}=0 \tag{39}$$

$$\frac{du^{\alpha}}{dt}=\frac{1}{\rho}\frac{\partial \sigma^{\alpha\beta}}{\partial x^{\beta}}+g^{\alpha} \tag{40}$$

where u denotes the velocity, g is the gravitational constant, and $\sigma^{\alpha\beta}$ is the total shear stress tensor in a fluidic approach that can be written as the isotropic pressure p and the viscous stresses τ

$$\sigma^{\alpha\beta}=-p\delta^{\alpha\beta}+\tau^{\alpha\beta} \tag{41}$$

where $\delta^{\alpha\beta}$ is Kronecker's delta function.

In the SPH formulation (Violeau, 2012), the Navier-Stokes equations can be approximated as

$$\frac{d\rho_i}{dt}=\rho_i\sum_{j}^{N}\frac{m_j}{\rho_j}(u_i^{\alpha}-u_j^{\alpha})\frac{\partial W_{ij}}{\partial x^{\alpha}} \tag{42}$$

$$\frac{du_i^{\alpha}}{dt}=\sum_{j}^{N}\left(\frac{\sigma_i^{\alpha\beta}+\sigma_j^{\alpha\beta}}{\rho_i\rho_j}\right)\frac{\partial W_{ij}}{\partial x^{\beta}}+g_i^{\alpha} \tag{43}$$

which are applied to each particle i in the domain.

To approximate an incompressible fluid, an equation of state (EOS) (Batchelor, 2000; Monaghan, 2005) is needed to link pressure to density. In this work, the following form is used:

$$p = B\left(\left(\frac{\rho}{\rho_0}\right)^{\gamma} - 1\right) \tag{44}$$

where ρ_0 is the reference density and B is based on the compressibility which is proportional to the speed of sound of the fluid as

$$B = \frac{C_{s0}^2 \rho_0}{\gamma} \tag{45}$$

and γ is the polytropic index which usually takes the value of 7 (Monaghan, 2000) and C_{s0} is the numerical speed of sound calculated as

$$C_{s0} \geq 10 u_{max} \tag{46}$$

where u_{max} is the maximum velocity magnitude in the domain.

Within *DualSPHysics*, it is also possible to apply a δ-SPH formulation, which introduces a diffusive term to reduce density fluctuations. The state equation describes a very stiff density field, and together with the natural disordering of particles, high-frequency low-amplitude oscillations will populate the density scalar field (Molteni and Colagrossi, 2009). *DualSPHysics* uses a diffusive term in the continuity equation, which has the form of

$$\frac{d\rho_i}{dt} = \sum_j m_j \mathbf{v}_{ij} \cdot \nabla_i W_{ij} + 2\delta_\Phi h C_{s0} \sum_j (\rho_j - \rho_i) \frac{\mathbf{r}_{ij} \cdot \nabla_i W_{ij}}{\mathbf{r}_{ij}^2} \frac{m_j}{\rho_j} \tag{47}$$

This represents the original δ-SPH formulation by Molteni and Colagrossi (2009), with the free parameter δ_Φ that needs to be assigned a suitable value. This can be explained as the addition of the Laplacian of the density field to the continuity equation. As for the value of coefficient δ_Φ, 0.1 is recommended for most applications.

In the SPH method, the wall boundary condition applied in this work is the dynamic boundary conditions (DBC) (Crespo et al., 2007) where particles representing the wall are organized in a staggered arrangement and satisfy the same equations as the fluid particles but their position and velocity are prescribed. The advantages of the DBC include the straightforward implementation and the treatment of arbitrary complex geometries. This makes them particularly suitable to be used within the GPU code *DualSPHysics* (Crespo et al., 2015).

The time stepping algorithm used in this work is an explicit second-order predictor-corrector integrator scheme. The scheme predicts the evolution in time at two half time steps. These values are then corrected using the forces at half time steps, followed by the evaluation of the values at the end time step (Gomez-Gesteira et al., 2012). The scheme is bounded by the Courant-Friedrichs-Lewy (CFL) condition, the maximum force term, and the numerical speed of sound as demonstrated by Monaghan (1989). In addition, an extra restriction is imposed based on the viscous forces. The CFL condition reads

$$\Delta t = Co_{min}\left(\min_i \sqrt{\frac{h}{|f_i|}}, \frac{h}{C_{s0}}, \frac{h^2}{\nu}\right) \tag{48}$$

where f_i is the force per unit mass of particle i and Co_{min} is the Courant number set to 0.3 in this work and ν is the kinematic viscosity. The same time integration scheme is used for both phases using the minimum Δt resulting from the CFL condition.

Fluid phase model: The fluid phase is treated as a simple Newtonian fluid and thus the Newtonian constitutive law is used. The viscous stresses $\tau_i^{\alpha\beta}$ are computed as

$$\tau_i^{\alpha\beta} = 2\mu\dot{\epsilon}_i^{\alpha\beta} \tag{49}$$

where μ is the dynamic viscosity of water and $\dot{\epsilon}_i^{\alpha\beta}$ is the deviatoric strain rate, defined as

$$\dot{\epsilon}_i^{\alpha\beta} = \frac{1}{2}\left(\frac{\partial u_i^{\beta}}{\partial x_i^{\alpha}} + \frac{\partial u_i^{\alpha}}{\partial x_i^{\beta}}\right) - \frac{1}{3}\frac{\partial u_i^{\gamma}}{\partial x_i^{\gamma}}\delta^{\alpha\beta} \tag{50}$$

where u denotes the velocity, Greek superscripts α and β denote coordinate directions by employing Einstein's summation, and $\delta^{\alpha\beta}$ is Kronecker's delta function.

The SPH approximation of Eq. 50 can be written as

$$\dot{\epsilon}_i^{\alpha\beta} = \frac{1}{2}\left(\sum_j^N \frac{m_j}{\rho_j} u_{ji}^{\beta}\frac{\partial W_{ij}}{\partial x_i^{\alpha}} + \sum_j^N \frac{m_j}{\rho_j} u_{ji}^{\alpha}\frac{\partial W_{ij}}{\partial x_i^{\beta}}\right) - \frac{1}{3}\left(\sum_j^N \frac{m_j}{\rho_j} u_{ji}^{\gamma}\frac{\partial W_{ij}}{\partial x_i^{\gamma\gamma}}\right) \tag{51}$$

This model has been validated for a range of free-surface flows as described in Fourtakas and Rogers (2016).

Sediment phase model: The solid state of sediment is assumed to have an isotropic linear behavior, which obeys a yield criterion. The deviatoric stress rate $\dot{\tau}^{\alpha\beta}$ are evaluated in line with the well-known elastic relations, i.e.

$$\dot{\tau}_i^{\alpha\beta} = \frac{E_y}{1+\nu_p}\dot{\epsilon}_i^{\alpha\beta} \tag{52}$$

where E_y denotes the Young's modulus and ν_p refers to the Poisson's ratio.

For large deformation of the sediment phase, a stress rate that is invariant with respect to rigid-body rotation must be employed. To obtain a material frame independent formulation, Eq. 52 is replaced by the Jaumann rate with respect to the elastic spin (Ulrich et al., 2013; Ghaïtanellis et al., 2018)

$$\dot{\tau}_i^{\alpha\beta} = \frac{E_y}{1+\nu_p}\dot{\epsilon}_i^{\alpha\beta} + \tau_i^{\alpha\gamma}\dot{\omega}_i^{\gamma\beta} - \dot{\omega}_i^{\alpha\gamma}\tau_i^{\gamma\beta} \tag{53}$$

where $\dot{\omega}_i^{\alpha\beta}$ denotes the spin-rate tensor

$$\dot{\omega}_i^{\alpha\beta} = \frac{1}{2}\left(\frac{\partial u_i^{\beta}}{\partial x_i^{\alpha}} - \frac{\partial u_i^{\alpha}}{\partial x_i^{\beta}}\right) \tag{54}$$

The final form of the adopted deviatoric stresses reads

$$\dot{\tau}^{\alpha\beta} = \frac{E_y}{1+\nu_p}\dot{\epsilon}^{\alpha\beta} + J^{\alpha\beta} - \frac{1}{3}J^{\gamma\gamma}\delta^{\alpha\beta} \tag{55}$$

where $J^{\alpha\beta}$ is the Jaumann rate.

The viscoplastic fluid state of sediment is considered to be fully saturated and is modeled as a slightly compressible pseudo-Newtonian fluid in line with the works of Fourtakas and Rogers (2016). The viscous term is obtained as a function of the apparent viscosity μ_{app} as

$$\tau_i^{\alpha\beta} = 2\mu_{app}\dot{\epsilon}_i^{\alpha\beta} \tag{56}$$

The apparent viscosity of the sediment is calculated using the Herschel-Bulkley-Papanastasiou (HBP) model (Papanastasiou, 2002). Thus, in this work the symbol μ_{HBP} is used to denote the apparent viscosity, i.e. $\mu_{HBP} = \mu_{app}$. The HBP model reads

$$\mu_{HBP} = \frac{\tau_c}{\sqrt{II_D}}\left[1 - e^{-\tilde{m}\sqrt{II_D}}\right] + 2\mu|4II_D|^{\frac{\tilde{n}-1}{2}} \tag{57}$$

where $\tilde{m}$ controls the exponential growth of stress and $\tilde{n}$ is a power-law index that enables simulation of shear thinning or shear thickening behavior. Note that when $\tilde{m} = 0$ and $\tilde{n} = 1$ the model reduces to a Newtonian model, whereas when $\tilde{m} \to \infty$ and $\tilde{n} = 1$ a simple Bingham model is recovered. The parameter τ_c is the yield stress that should be defined by a yield criterion. The advantage of the HBP model is that it provides information on the pre-yield and post-yield region and thereby avoids the need of setting a maximum threshold for the viscosity as required in other pseudo-Newtonian approaches.

Drucker-Prager yield criterion: To determine the state of the sediment SPH particle (yielded or unyielded), a yield criterion is used to relate the maximum shear strength of the soil sediment to the hydrodynamic shear strain at the fluid-soil interface. Note that compression is assumed to be positive. Considering a simple shear case where no motion in the sediment phase takes place until a critical value of shear stress τ_y (Bingham yield stress) is reached, the fluid stresses acting on the sediment are in equilibrium with the yield strength of the sediment (Fourtakas et al., 2013), i.e.

$$\sqrt{J_2} - \left|\tau_y\right| \geq 0 \tag{58}$$

where J_2 is the second invariant of the deviatoric shear stress tensor $\tau^{\alpha\beta}$ defined as

$$J_2 = \frac{1}{2}\tau^{\alpha\beta}\tau^{\alpha\beta} \tag{59}$$

The rate-dependent isotropic Newtonian fluid expression for the viscous stresses is written as

$$\tau^{\alpha\beta} = 2\mu\dot{\epsilon}^{\alpha\beta} \tag{60}$$

Then the following equality is obtained

$$\sqrt{J_2} = 2\mu\sqrt{II_D} \tag{61}$$

where the term II_D is the second invariant of the strain rate tensor defined as

$$II_D = \frac{1}{2}\dot{\epsilon}^{\alpha\beta}\dot{\epsilon}^{\alpha\beta} \tag{62}$$

Thus, the critical threshold for the sediment yielding at the interface can be written as

$$\left|\tau_y\right| < 2\mu\sqrt{II_D} \tag{63}$$

At this point, a yield criterion for the sediment phase is needed to provide the critical value of the sediment shear stress. In this study, the Drucker-Prager yield criterion is selected. The Drucker-Prager model (Drucker and Prager, 1952) is written in a general form as

$$\sqrt{J_2} - \alpha_\phi I_1 - \kappa_c = 0 \tag{64}$$

where I_1 is the first invariant of the deviatoric shear stress tensor. The parameters α_ϕ and κ_c can be determined by projecting the Drucker-Prager (DP) onto the Mohr-Coulomb yield criterion in a deviatoric plane:

$$\alpha_\phi = \frac{\tan(\phi_0)}{\sqrt{9 + 12\tan^2(\phi_0)}} \quad \kappa_c = \frac{3c}{\sqrt{9 + 12\tan^2(\phi_0)}} \tag{65}$$

where ϕ_0 is the angle of repose and c is the cohesion of the sediment.

Finally using Eq. 63 yielding will occur when the following equation is satisfied

$$\alpha_\phi I_1 + \kappa_c < 2\mu\sqrt{II_D} \tag{66}$$

Sediment suspension: At the interface, the fluid flow at a sufficiently large velocity ($\tau_y \ll \tau_{fluid}$) will suspend the sediment particles in the fluid. This sediment entrainment by the fluid can be controlled by using a concentration volume fraction of the mixture c_ν

$$c_{\nu,i} = \frac{\sum_{j_{sat}\in 2h}^{N} \frac{m_j}{\rho_j}}{\sum_{j\in 2h}^{N} \frac{m_j}{\rho_j}} \tag{67}$$

where the summation is defined within the support of the kernel and j_{sat} refers to the yielded saturated sediment particles. The size of the concentration sampling is chosen as to adhere with the kernel support size of SPH. When a sediment particle is suspended, it is modeled as a pseudo-Newtonian fluid using Eq. 56. The suspension viscosity can be related to the volumetric concentration by

$$\mu_{susp} = \mu f\left(c_\nu\right) \tag{68}$$

A suspension viscosity is used based on the Vand experimental colloidal suspension equation (Vand, 1948) of sediment in a fluid by

$$\mu_{susp} = \mu e^{\frac{2.5c_\nu}{1-\frac{39}{64}c_\nu}} \quad c_\nu \leq 0.3 \tag{69}$$

assuming an isotropic material with spherically shaped sediment particles. Eq. 69 is applied only when the volumetric concentration of the saturated sediment particle within the SPH kernel is lower than 0.3 which is the upper validity limit of Eq. 69. Hence, when a yielded sediment particle volumetric concentration is below the threshold of 0.3 which coincides with the validity of the Vand equation, the sediment particle is treated as a Newtonian fluid, retaining its properties with the exception of the viscosity that follows the Vand Eq. 69.

3.2.3 Munition 6-DoF motion domain

To compute the motion of a moving body with 6-DoF, rigid-body dynamics should be solved (Monaghan, 2005). The basic equations of rigid-body dynamics can be written as follows:

$$M\frac{d\mathbf{V}_b}{dt} = \sum_k m_k \mathbf{f}_k \tag{70}$$

$$I\frac{d\mathbf{\Omega}_b}{dt} = \sum_k m_k(\mathbf{r}_k - \mathbf{R}_0) \times \mathbf{f}_k \tag{71}$$

where M is the mass of the object, I is the moment of inertia, $\mathbf{V}_b$ is the velocity of the rigid-body, $\mathbf{\Omega}_b$ is the rotational velocity of the body, and $\mathbf{f}$ is the net force acting on each particle at the solid boundary. The net force on each boundary particle can be calculated by all surrounding fluid particles referenced by the kernel function and the smoothing length. $\mathbf{R}_0$ is the center of the object and k indicates the boundary particle on the rigid-body surface. Thus, force contributions on the entire rigid-body are summed. After calculating the velocity and the rotational velocity of the rigid-body, the velocity of each particle $\mathbf{v}$ on the rigid-body surface can be updated as follows:

$$\mathbf{v} = \mathbf{V}_b + \mathbf{\Omega}_b \times (\mathbf{r} - \mathbf{R}_0) \tag{72}$$

4 RESULTS AND DISCUSSION

The models described above have been verified and validated. Some preliminary simulations for the munition dynamics have been performed. In this result section, these validation and simulation cases will be presented.

4.1 CFD domain results

This section is divided into three parts. The first part is to show the hydrodynamic results, which is the emphasis of the project period up until this point. Validation cases for the proposed immersed boundary method, including 1D, 2D, and 3D cases, are presented. The second part will show the results with the newly proposed sand slide algorithm, which is a key part of the scour model. In part three, some preliminary 3D scour simulations around both fixed and moving munitions will be presented.

4.1.1 Hydrodynamic results

1D open channel flow case: A simple 1D channel flow case with water is used to test the proposed rough IB wall function. The mean velocity U is 0.5 m/s, channel depth H is 1 m, and the Reynolds number $Re = UH/\nu = 5 \times 10^5$. Figure 9 shows the velocity distributions in the channel with different roughness height k_s and the comparison with theoretical distribution. Good agreement can be observed.

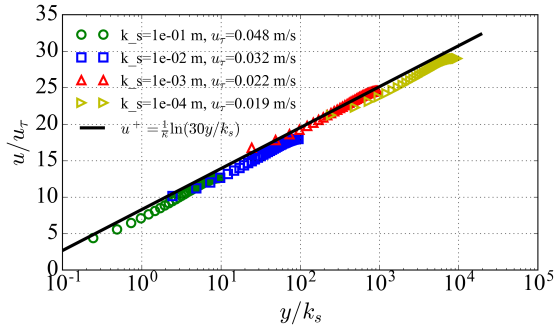

Figure 9: Simulated velocity distributions in 1D channel with different roughness height using the proposed rough IB wall function. Here, $u^+ = u/u_\tau$.

Pitz-Daily 2D case: The 2D Pitz-Daily case is a classic backward facing step case commonly used to evaluate the performance of turbulence models (Pitz and Daily, 1981). The flow is assumed as incompressible. The mean inlet velocity is $U = 13.3$ m/s, step height $H = 0.0254$ m, kinematic viscosity is $\nu = 1.5 \times 10^{-5}$ m/s^2, where Reynolds number is $Re = UH/\nu = 2.2 \times 10^4$. It is used here as a validation case to compare with results from experiments and simulation with a body-fitted mesh. The case was also simulated with the IB method reported in Jasak et al. (2014) and Jasak and Tuković (2015). There are two major differences between the present IB method and theirs. One is that there is no y^+-adaptation process in their method. The second is that in their $k - \epsilon$ turbulence model, the gradient of both k and ϵ are fixed as zero on the IB faces.

The mesh used with immersed boundary methods has a total of 15,000 cells and the body-fitted mesh has 12,225 cells. The resolutions of both meshes are comparable and they are plotted in Figure 10. The mesh for the immersed boundary methods uses a uniform background mesh with no local refinement. The red cells are the IB cells for the upper and lower walls at the end of simulation, which have already been modified with the y^+-adaptation algorithm. The contraction of the outlet leads to the stair-like arrangement of IB cells, which is very common in the use of immersed boundary method. For the body-fitted mesh, there is some refinement near the walls and in the zone of shear layer downstream of the step.

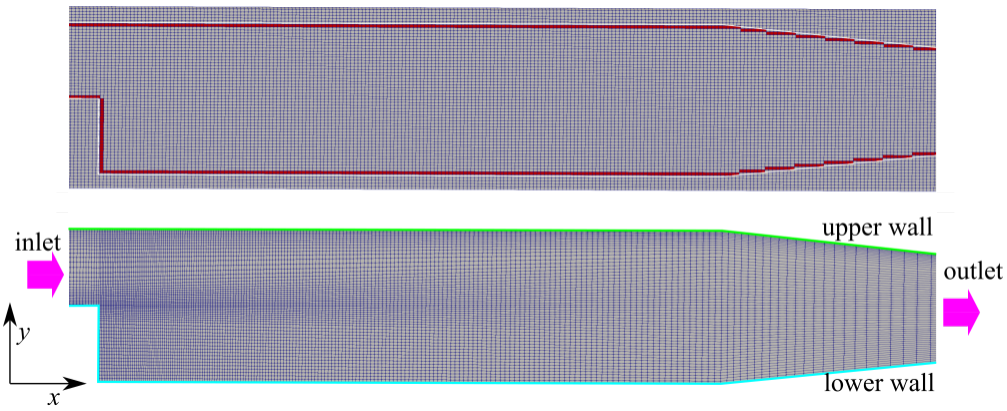

Figure 10: The mesh for immersed boundary methods (upper) and the body-fitted mesh (lower). The red cells in upper mesh are the IB cells.

At the inlet, the boundary conditions for $\mathbf{u}$, k and ϵ are prescribed using experimental data from (Pitz and Daily, 1981). At the outlet, pressure is fixed as zero and the boundary conditions for all other variables are zero gradient. Wall functions are applied to the upper and lower walls.

Figure 11 shows the comparison between the experiment and simulations. Overall, the present IB method gives satisfactory results. Specifically, as seen in Figure 11a for streamwise velocity, though the present method is slightly off in comparison with experimental data, it gives almost the same result as the simulation with a body-fitted mesh. The IB method in Jasak et al. (2014) gives less ideal result where the re-circulation in the wake zone is weaker than the body-fitted mesh and present IB methods. This might be induced by the zero gradient condition applied to IB faces in Jasak et al. (2014). In Figure 11b and Figure 11c for k and ϵ, the IB method in Jasak et al. (2014) overestimated their value in the wake, especially in the shear layer. The contour, which is not presented here, shows that there are some cells with excessively large values of k at the corner of the step where shear layer starts to form. These large values are not observed in the results with a body-fitted mesh or the present IB method. This might again be caused by the zero gradient condition for k applied on IB faces in Jasak et al. (2014). In Figure 11d for the eddy viscosity, the present IB model agrees with body-fitted mesh simulation while the IB method in Jasak et al.

(2014) overestimated the level of eddy viscosity.

It is also noted that in Figure 11c for ϵ, in some near wall region, ϵ appears to be smaller in IB method than body-fitted mesh. This is caused by different calculation locations of boundary value in these two methods. In the wall function with body-fitted mesh, ϵ is evaluated at boundary cell center. However, in IB method, ϵ is evaluated at IB cell center. According to Eq. (33), the calculated ϵ at a boundary is very sensitive to the wall distance y (smaller y leads to larger numerical value of ϵ). Due to the y^+-adaptation scheme, the IB cell centers are in general far away from the solid wall, thus the IB cells' ϵ values are smaller. Despite the visual difference in the ϵ distribution, the bulk flow behavior from the IB method is comparable with the body-fitted mesh method.

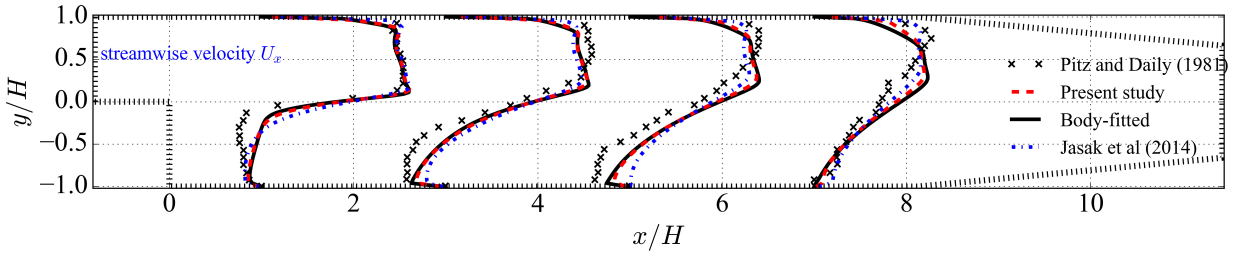

(a) streamwise velocity U_x

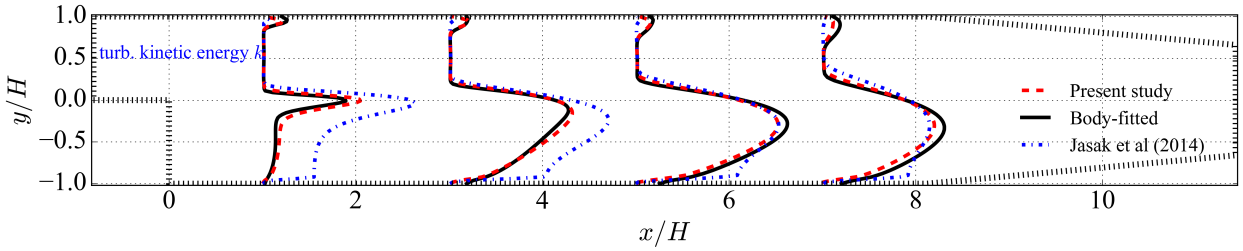

(b) turbulent kinetic energy k

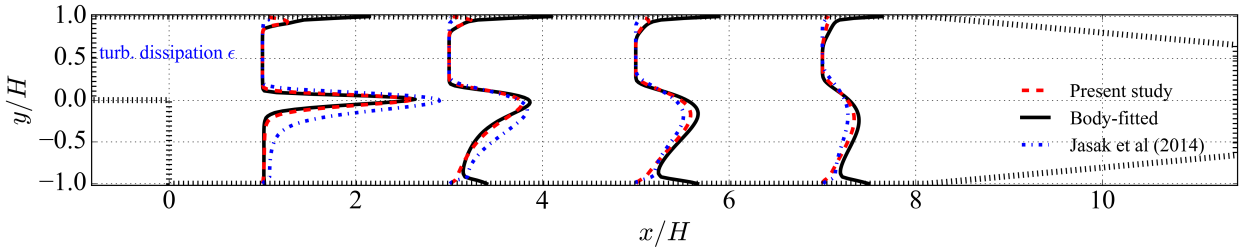

(c) turbulent dissipation ϵ

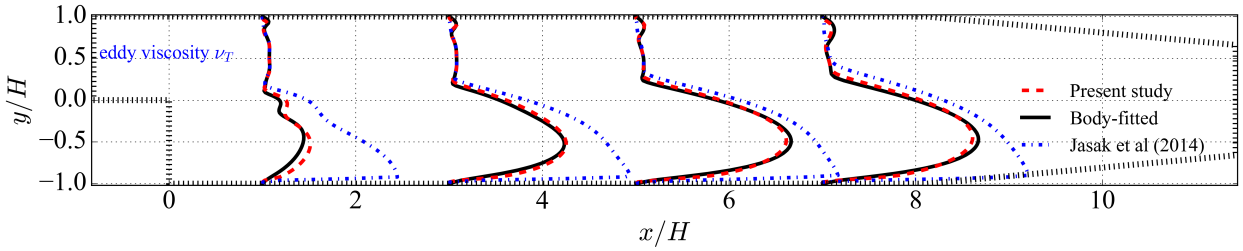

(d) eddy viscosity ν_T

Figure 11: Comparison of results among the present IB method, the IB method in (Jasak et al., 2014), and simulation with a body-fitted mesh, and experiments in Pitz and Daily (1981). The flow is from left to right.

The two oblique wall boundaries near the outlet are the perfect location to show the capability of the proposed y^+-adaptation scheme. For comparison, another case without the y^+-adaptation was also simulated. The resulted distributions of wall shear stress are shown in Figure 12. The wall shear stress distribution is plotted using line or scatters in which their distance to the wall is proportional to the magnitude of wall shear. The sign of the wall shear (positive in the x-direction) is represented by whether the line or scatters are located inside (positive) or outside (negative) of the domain. It is noted that the magnitude of wall shear from the IB method in Jasak et al. (2014) is divided by 10^3 so the spikes can be plotted within the figure.

The insert in Figure 12 is a close-up view of the shear stress along the lower wall. It can be observed that without y^+-adaptation, the wall shear distribution is not as smooth and has a semi-periodic abnormality. The abnormality is located at IB cells whose wall distances are small. The periodicity is due to the fact that the background mesh is uniform and the lower wall is an oblique line. As a result, the IB cell distribution without y^+-adaptation along the lower wall is stair-like (see IB cells bounded by yellow lines in Figure 13). On the hand, the y^+-adaptation method significantly reduces the abnormality and thus increases the smoothness in wall shear.

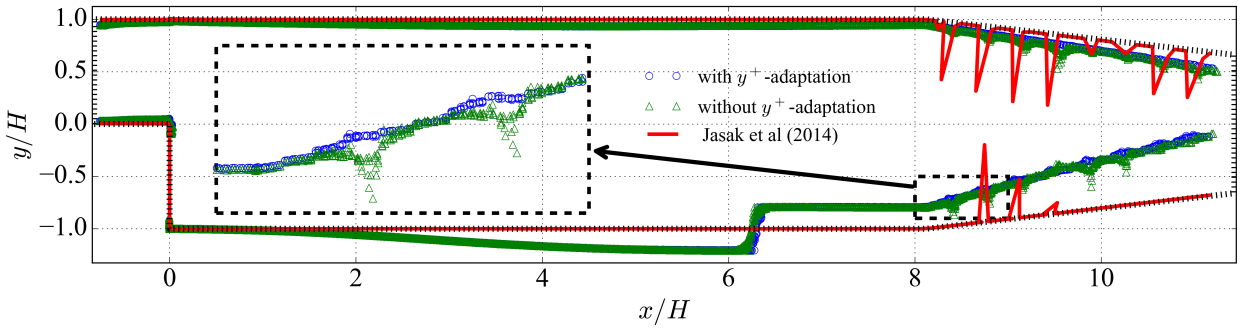

Figure 12: Wall shear stress distribution along the lower and upper walls.

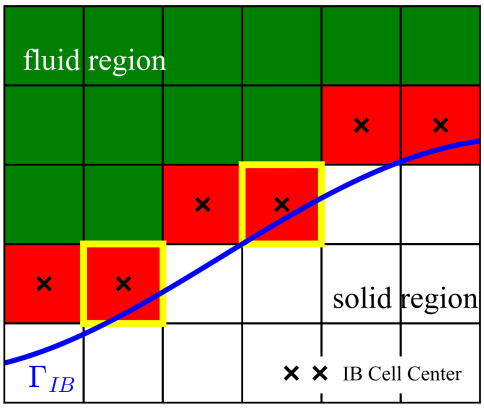

Figure 13: Schematic view of step IB cells, which are highlighted by yellow frames. IB cells (red filled), live cells (green filled), and dead cells (white filled). Immeresed interface Γ_{IB} is represend by the blue curve.

Flow around 3D cylinder: To validate the new IB method, the CFD model was used to simulate the turbulent open channel flow over a 3D cylinder and compared with the experimental study in Roulund et al. (2005). The vertical cylinder was modeled with body-fitted mesh, while the flat and rough bed was modeled with the IB method (Figure 14). This is a common setup for the purpose of scour simulation. The case

parameters and flow conditions are listed in Table 1. To validate the hydrodynamic part of our model, the bed was fixed and no sediment transport was included. The blue and red lines in Figure 15 represent the time-averaged velocity in upstream and downstream regions at different vertical position, respectively. Both upstream and downstream velocities match well with the experimental data. The horseshoe vortex system in the front of cylinder (negative velocity of upstream) and flow separation in the wake region (negative velocity of downstream) are captured.

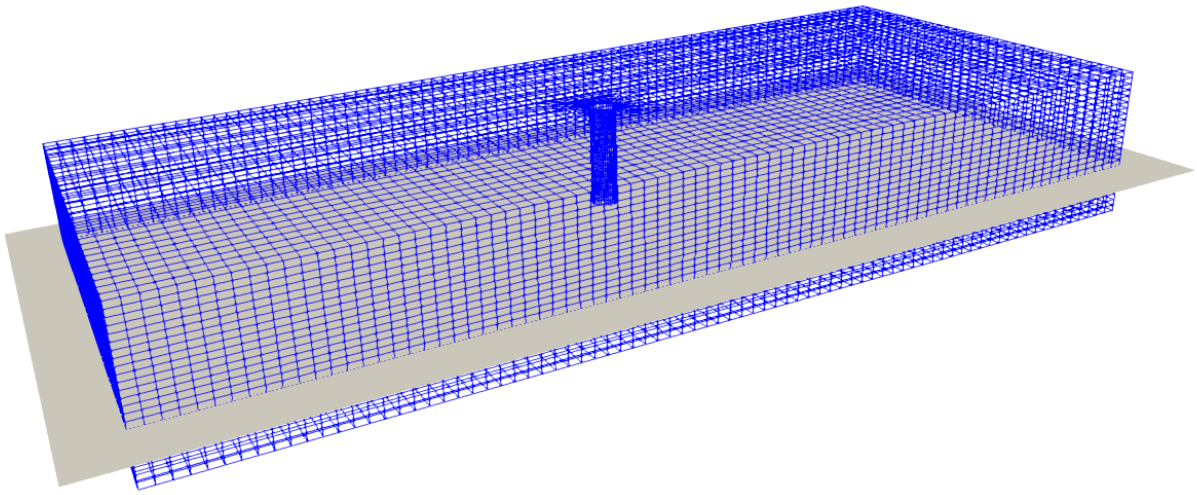

Figure 14: Schematic showing the mesh of flow around a vertical circular cylinder. Blue grid is the 3D hydrodynamics background mesh and grey board is the rough bed.

Table 1: Test conditions and meshes for flow around cylinder cases.

Bed type	Rigid-bed
Model selection	hydrodynamics only
Model type	IBM
Water depth H (cm)	54
Boundary layer thickness δ (cm)	54
Mean flow velocity U (cm/s)	32.6
Cylinder diameter D (cm)	53.6
Roughness height k_s (cm)	1.0
Shear velocity u_τ (cm/s)	2.3
3D background mesh (IBM)	
Mesh resolution (cm)	$1 \sim 4$
2D surface mesh size	
Mesh resolution (cm)	$2 \sim 8$

4.1.2 Sands slide simulation results

To validate the new sand slide algorithm proposed in this project as part of the 3D scour model, it was applied to solve the collapse of a sand cylinder ($r_0 = 5\ cm$ and $h_0 = 6\ cm$) as shown in Figure 16. In this case, the sand slide algorithm is separated from the rest of the scour model to highlight its features

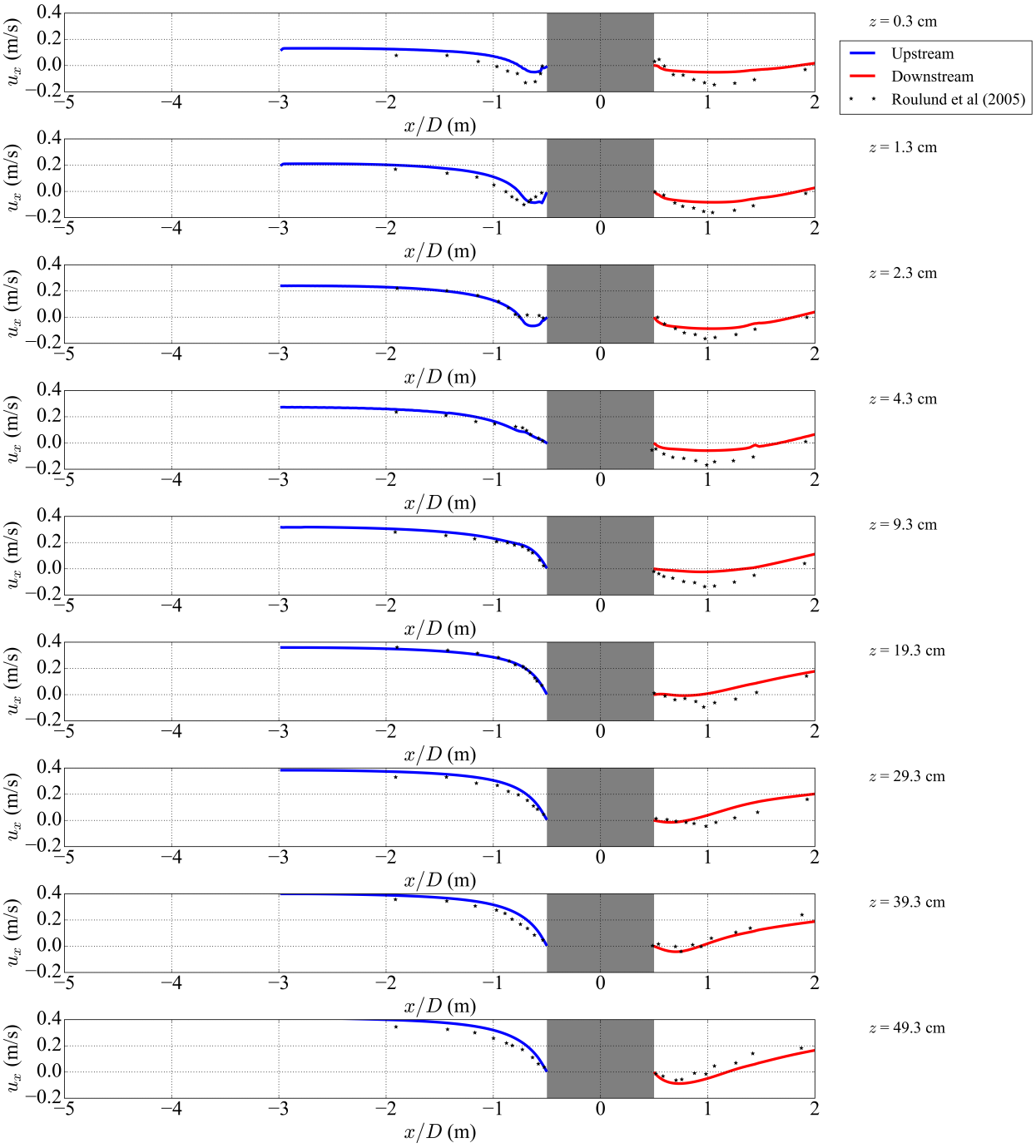

Figure 15: Flow around a vertical circular cylinder on a rough bed.

and capabilities. Thus, flow and sediment transport were not simulated. The angle of repose was set as 35° ($\tan\phi_0 = 0.7$). According to the definition of the angle of repose, this sand cylinder will collapse to a sand cone that has the same amount of sand as the sand cylinder. The bottom angle of the sand cone will be equal to the angle of repose. In the experiments of sand cylinder collapse reported in Lube et al. (2004), the cone after collapse will have a bottom angle that is slightly less than (about 3°~5°) the angle of repose, which depends on the initial aspect ratio of the sand cylinder $a = h_0/r_0$. This is because of the inertia associated with the collapsing, which is not included in the current sand slide model. However, this process is deemed not as important because in scour holes, the collapsing will not be significant.

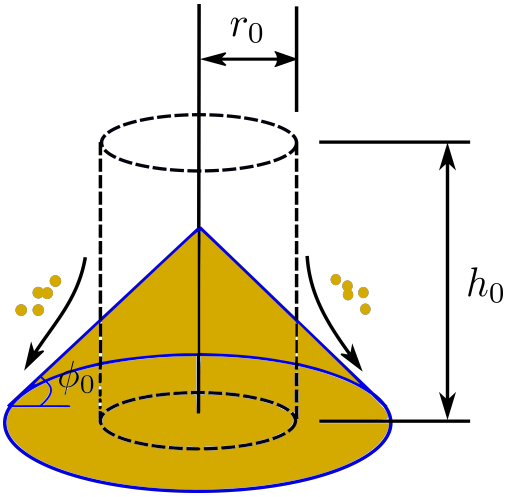

Figure 16: Schematic showing the sand slide of a sand cylinder

When the sand slide algorithm was initially developed, it was found that the results depended on the mesh type. It is of course not correct. The reason for the initial mesh dependence was identified as the interpolation scheme within the framework of finite volume method. Sand flux will be biased in certain directions when a traditional interpolation scheme involving only the two cells sharing one face. To correct this, a much bigger interpolation stencil should be used. In the following part, we will prove this mesh type independence of the final sand slide algorithm.

The sand slide case was simulated on four types of mesh as shown in Figure 17. The average mesh size for all mesh types are $\Delta x \approx 0.5$ cm. The time step was $\Delta t = 0.001$ s and the diffusivity was $K = 0.001$. The time step and the diffusivity control how much sand per area will slide to its downslope neighbors in one time step, i.e., $\Delta sand = \Delta t K \nabla z_b$. The upper limit of time step Δt and diffusivity K are thus constrained by $\Delta sand$, which is the amount of sand needed to reduce the bed slope to be below the angle of repose. There is probably no lower limit on time step because the smaller time step Δt and diffusivity K, the slower the bed slope will change toward equilibrium. However, the smaller product of $\Delta t K$ will increase the computational time.

Figure 18 shows the contour of sand slide results on different meshes. The profiles and slopes of these sand piles are plotted in Figure 19. The results on different meshes are cones and their angles are approximately close to the angle of repose, which shows that the new algorithm works correctly.

4.1.3 Scour modeling results around fixed munition

In this case, the munition is fixed in space and has no movement. This preliminary simulation case is to demonstrate the capability of the 3D scour model when munition's movement is minimal. The munition

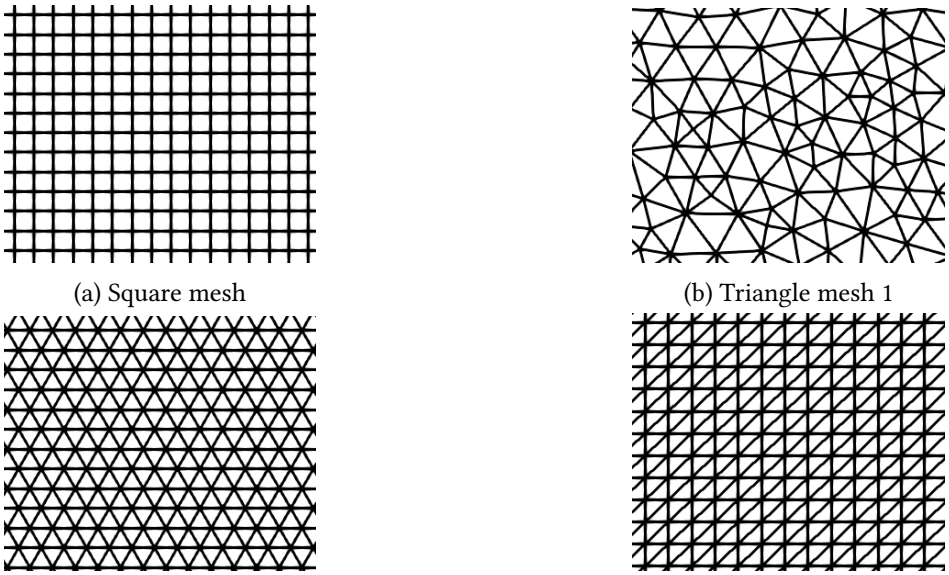

(a) Square mesh (b) Triangle mesh 1

(c) Triangle mesh 2 (d) Triangle mesh 3

Figure 17: Illustration of four mesh types: (a) Square mesh, (b) Triangle mesh 1, (c) Triangle mesh 2, (d) Triangle mesh 3.

has a body and four fins. It was created based on one of the munitions of interest to the SERDP Munition Response Program. It is placed in the domain with 25% burial as shown in Figure 20. The simulation domain is a rectangular channel with the inlet velocity being 0.5 m/s. The sediment has a mean size of 0.26 mm and thus the bed is live under this flow condition.

Figure 21 shows the bed scour pattern adjacent to the fixed munition with different angles of attack at equilibrium state. The simulation results clearly show that the orientation of munition has great influence on the bed morphodynamics and consequently the munition movement. It is clear that the munition will be pushed by the flow from the deposition region to the erosion region, i.e., the scour hole. When the munition is aligned with the flow direction, i.e., angle of attack = 0° and 180°, the scour pattern is symmetric with respect to the center line of munition. Thus, the munition may settle into one of the two scour pits without rolling away. For other angles of attack cases in Figure 21, the bed elevation change is not symmetric around the munition. The munition is more likely to be pushed downstream and roll into the scour hole in the wake or at the two ends.

To show the representative scour burial of fixed munition, 3D views of scour development for the angle of attack = 45° case at different time is shown in Figure 22. At the beginning, the undermining starts at the fin and head of munition where local flow velocity changes rapidly. Sand from upstream of the fin deposits in its downstream and accumulates there. Then, the scouring continues around the body of munition. Finally, the fin and the adjacent body are buried in the sand (see time = 16.7 min).

Figure 23 shows the time history of maximum depth of scour hole and deposition with different angles of attack. The scour pattern of all angles reaches equilibrium in about 1000 seconds. When the munition is aligned with the flow direction (angle of attack = $0^\circ, 180^\circ$), the depth of scour hole and deposition are relatively small because of the blockage induced by the munition is less. In other angles of attack, the munition is deeply buried and may become unstable if its 6-DoF motion is included.

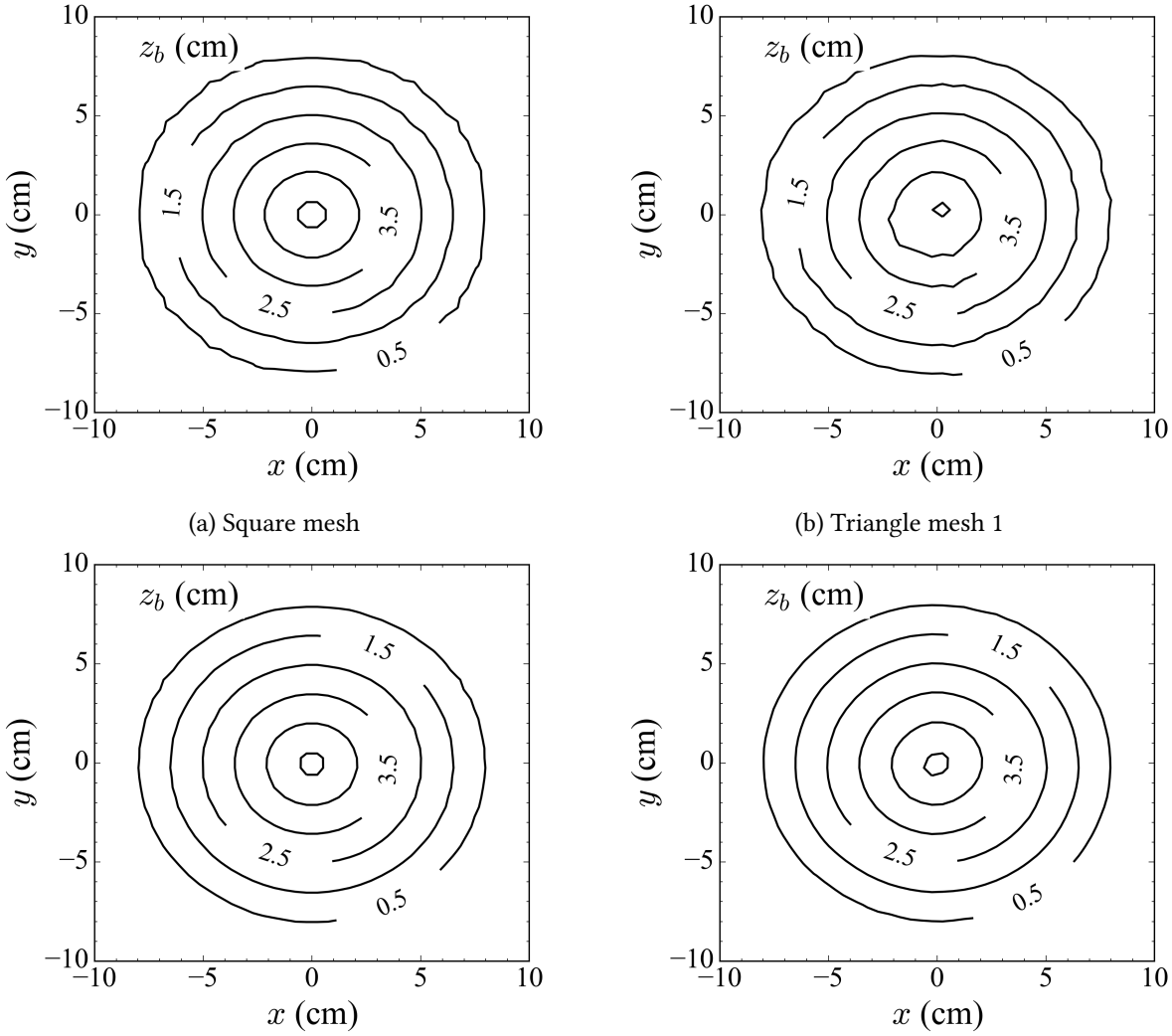

(a) Square mesh

(b) Triangle mesh 1

(c) Triangle mesh 2

(d) Triangle mesh 3

Figure 18: Contours of the sand piles on different meshes after sand side: (a) Square mesh, (b) Triangle mesh 1, (c) Triangle mesh 2, (d) Triangle mesh 3.

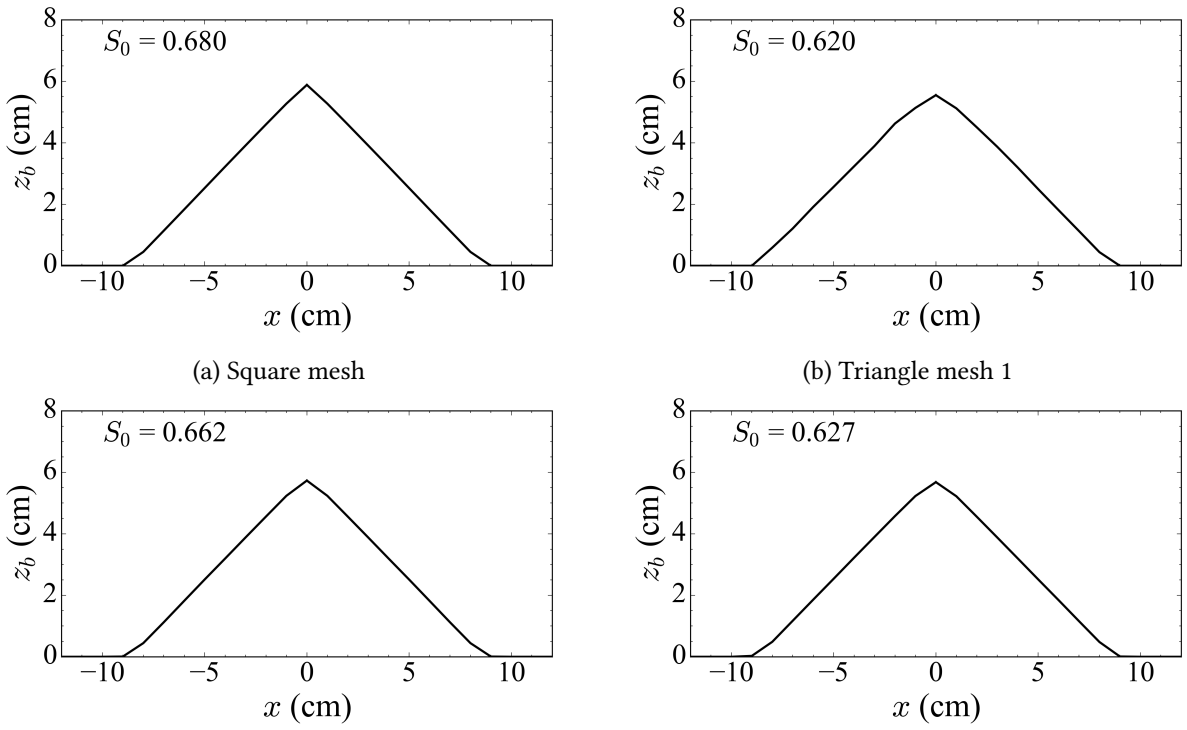

(a) Square mesh

(b) Triangle mesh 1

(c) Triangle mesh 2

(d) Triangle mesh 3

Figure 19: Profiles of the sand piles on different meshes after sand slide: (a) Square mesh, (b) Triangle mesh 1, (c) Triangle mesh 2, (d) Triangle mesh 3. S_0 is the slope of each profiles.

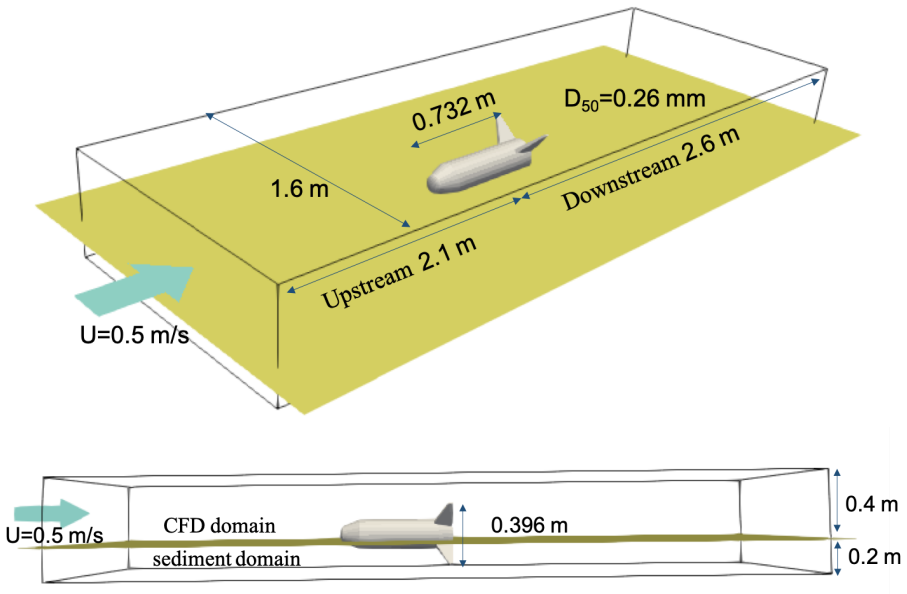

Figure 20: Schematic view of computational domain for scour around fixed munition.

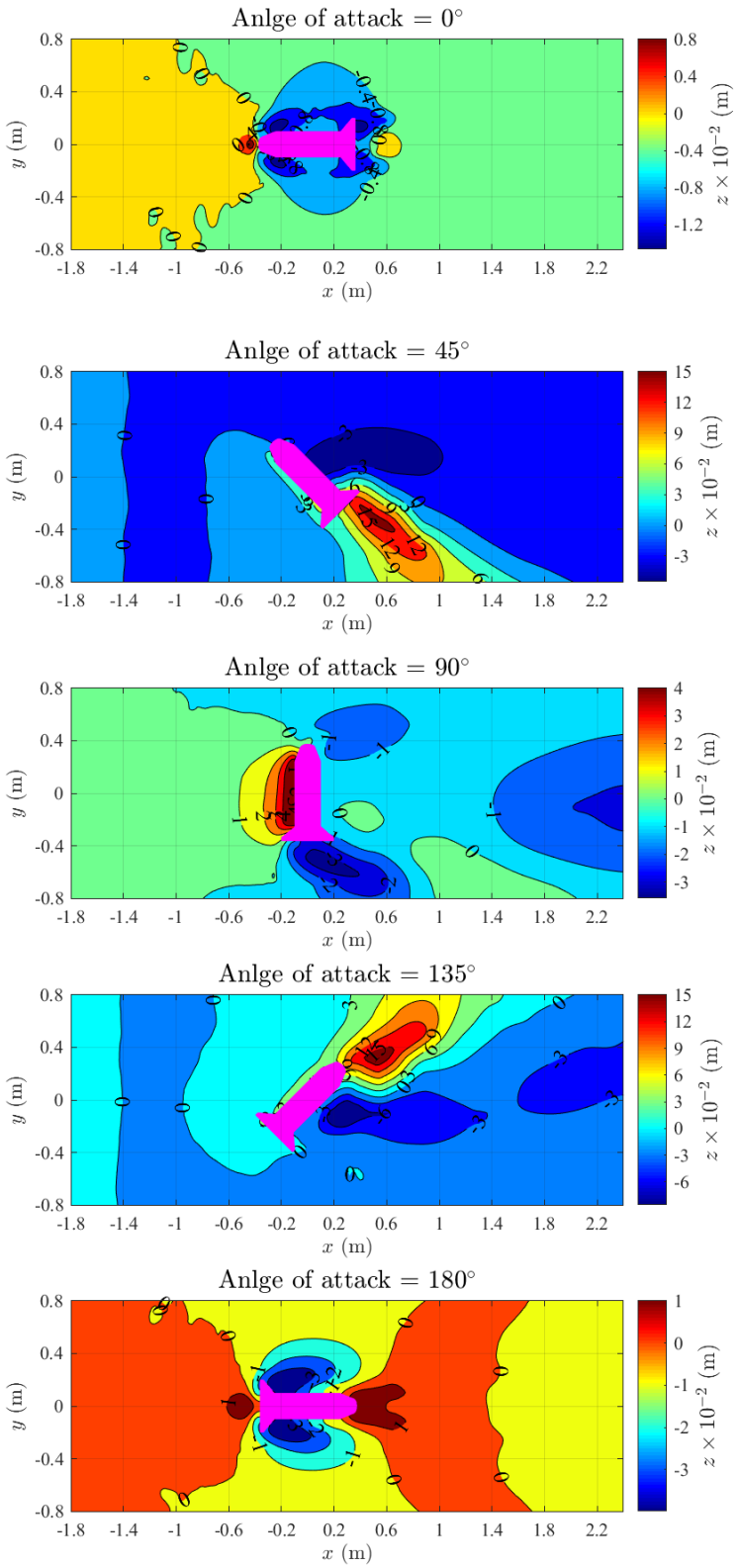

Figure 21: Scour pattern of fixed munitions with different angles of attack.

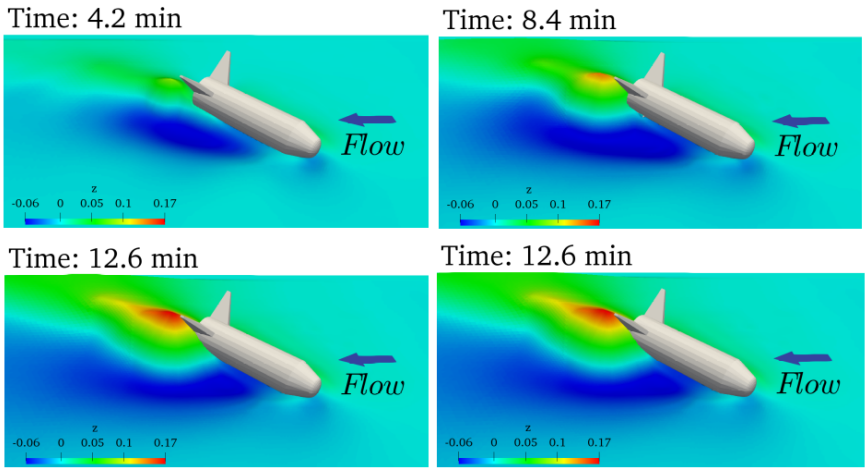

Figure 22: Representative scour burial of fixed munition with angle of attack = 45°

4.1.4 Scour modeling results of moving munition

In this case, to show that the 3D scour model can indeed handle the motion of munition, a prescribed motion was used to change the position of the munition during the simulation. In the future, the update of the munition position and orientation can be provided by the SPH model. This case is similar to the previous one except the munition's geometry is simpler and without the fins at the tail. The bed and the munition object are both modeled as an immersed boundary to handle the movement and the interactions between the two. The inlet velocity is 0.5 m/s and sand diameter is 0.5 mm. The prescribed motion lowers the munition with a velocity of (0,0,0.8 mm/s) and stops after 50 s as shown in Figure 24. The total lowering of the munition is then 40 mm (in comparison to its diameter of 58 mm). Three angles of attack, i.e., 0, 45, and 90 ° were simulated.

Figure 25 shows the bed scour pattern adjacent to the moving munition with different angles of attack at equilibrium state. The pre-described motion only exists in the vertically direction. Thus the scour patterns of the moving munition are very similar to those of the fixed munition in Figure 21, except that the scoured bed appears rougher. This is probably due to flow instability caused by the motion of munition.

As an example, Figure 26 shows the 3D views of the moving munition and deforming bed when angle of attack = 45°. The undermining again begins at the tip and continues laterally to the body, similar to the case with fixed munition. However, the difference is that in the case here the munition keeps sinking into the bed and thus the space for the undermining decreases with time.

4.2 SPH flow-object-sediment domain results

To validate and demonstrate the SPH model, several cases will be presented. First, a classic 2D sediment dam break experiment was simulated for the validation of the granular material behavior model. The second case is a 3D penetrometer experiment which not only has all the measurement data for comparison but also resembles the initial deployment of munitions. The third case is to show that the SPH model can also simulate the behavior of cohesive sediment. The fourth case is the munition mobility under cyclic loading and for the demonstration on the importance of munition density. The last case is the munition dynamics under dam break wave action. Some of these cases were analyzed in depth because the experimental data are available, while others are only briefly demonstrated.

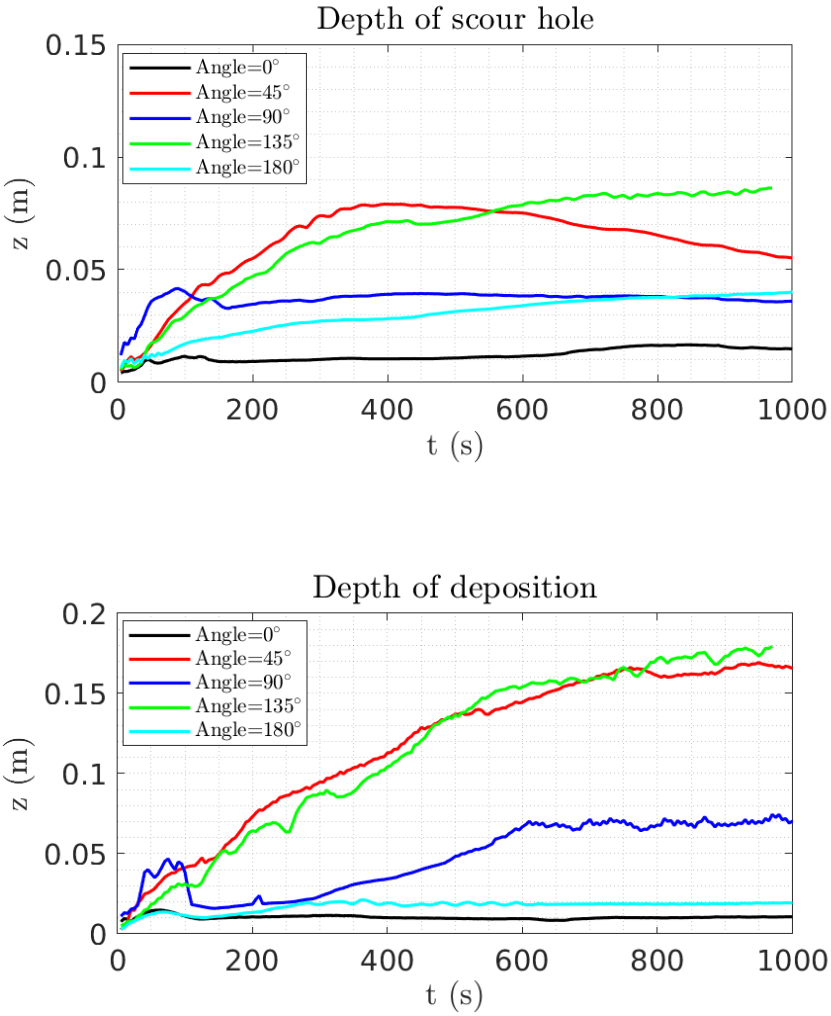

Figure 23: Depth of scour hole and deposition with different angles of attack.

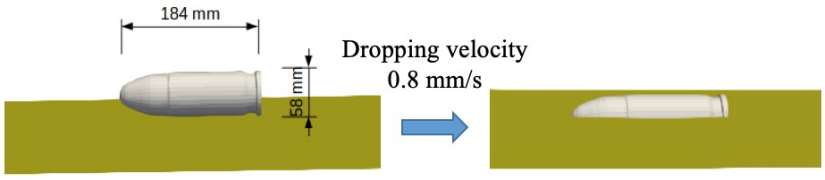

Figure 24: Schematic view of moving munition scour simulation.

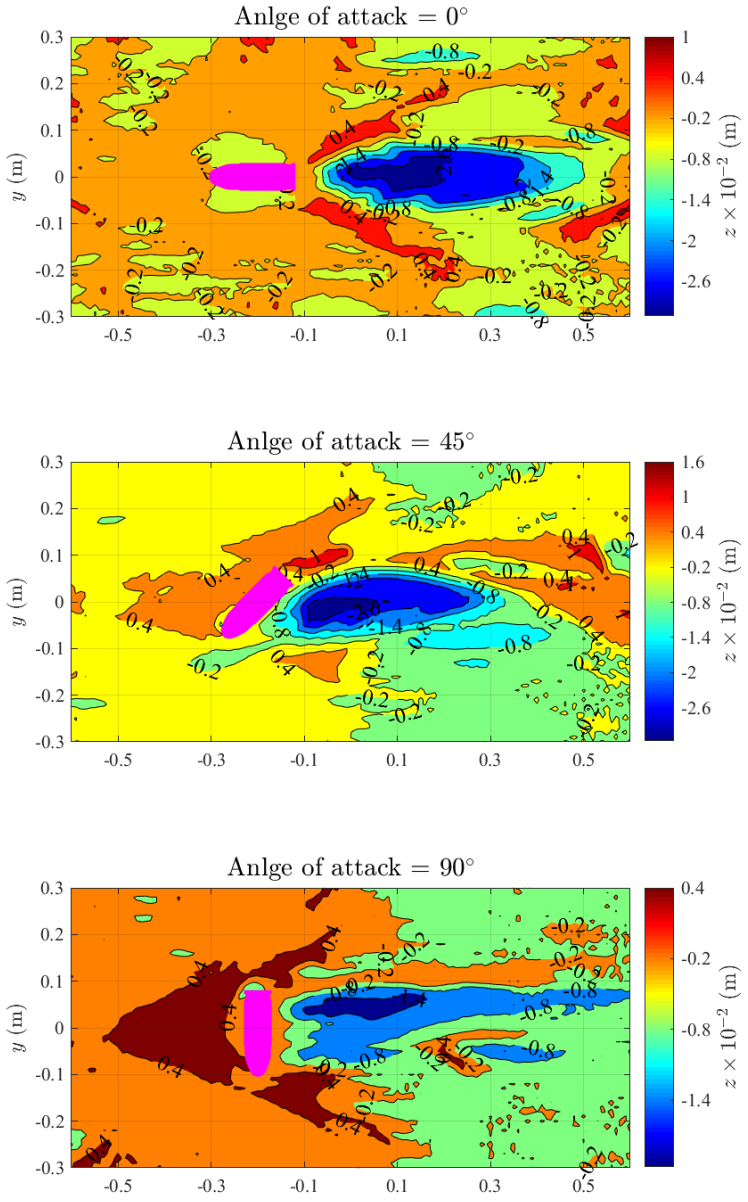

Figure 25: Scour pattern of moving munitions with different angles of attack.

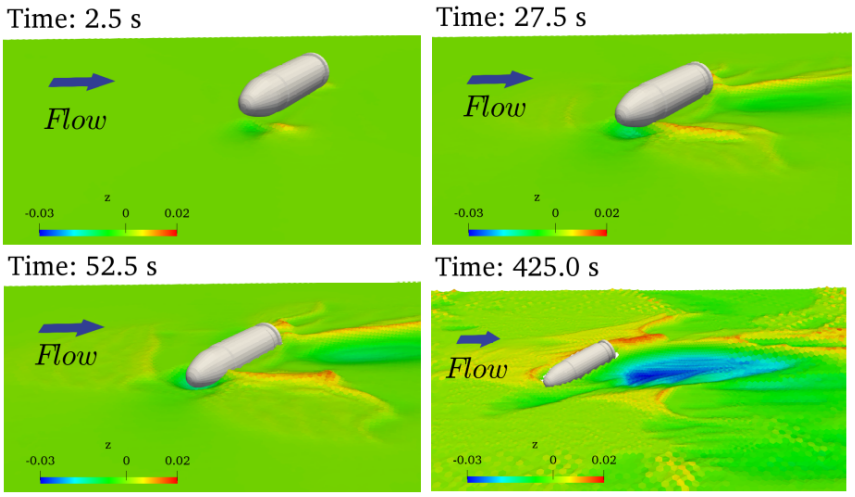

Figure 26: Representative scour burial of moving munition with angle of attack = 45°

4.2.1 Two-dimensional sediment dam break

This is a classic case for the validation of granular material behavior. Bui et al. (2008) conducted a series of 2D dam break experiments with small aluminum bars of diameters of 1 mm and 1.5 mm, length 50 mm , and density of $\rho = 2,650\ kg/m^3$ to model the cohesionless soil. The soil model was initially arranged into a rectangular box of 200 mm by 100 mm by 50 mm. The aluminum bars were supported by a wall and the dam break was triggered by quickly removing the wall horizontally to allow the collapse of bars. To model the experiments, Bui et al. (2008) also used a SPH model based on the Drucker-Prager constitutive relationship and non-associated flow rule to describe the soil behavior under flow-type failure. The experimental and numerical results of Bui et al. (2008) have been used to validate numerous codes for modeling large deformation of geomaterials (Chen et al., 2011; Zhang et al., 2014; Mast et al., 2014; Fern and Soga, 2016). Noteably, Fourtakas and Rogers (2016) conducted SPH simulation of the experiments by treating the soil (i.e., aluminum bars) as a visco-plastic material.

The current SPH model improves the work of Fourtakas and Rogers (2016) by incorporating an elasticity term in the treatment of the soil. Hence, a comparison between the simulations in Fourtakas and Rogers (2016) and the present study would highlight the improved capability. Parameters for this case are summarized in Table 2. Figure 27 shows both the SPH models of Fourtakas and Rogers (2016) and the present study can successfully capture the yield zone and final deposit profile. For the yield zone, the results from both models are almost identical because the same yield criteria were used. For the final deposit profile, the present study yielded better match with the experimental results, highlighting the benefit of incorporating the elastic behavior of the soil into the constitutive relationship.

Table 2: Parameters for 2D dam break.

Sand	$E_y(MPa)$	ν_p	$c(KPa)$	$\phi_0(\circ)$	$\tilde{m}$	$\tilde{n}$	μ	specific gravity
Value	0.84	0.3	0	19.8	100	1.2	0.002	2.65

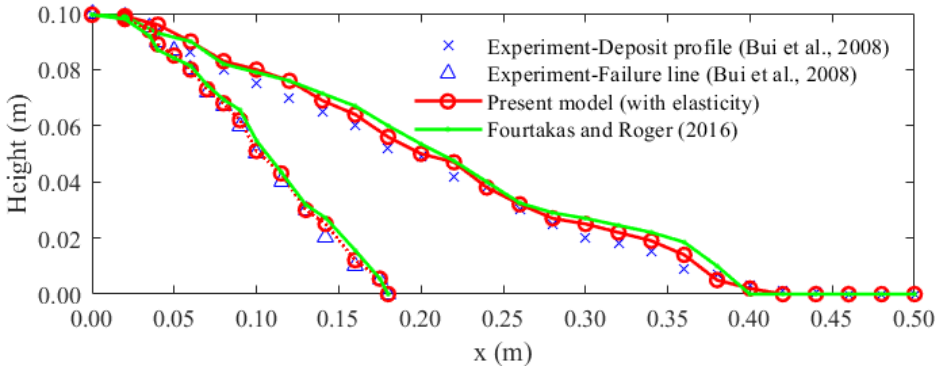

Figure 27: Comparison between experimental and simulation results for 2D dam break.

4.2.2 Three-dimensional Penetrometer Experiment and Simulation

The *blueDrop* device is a portable free-fall penetrometer (Stark, 2016), which is shown in Figure 28 and can be used to collect in-situ measurements of surficial sea floor sediments. This small lightweight penetrometer is highly suitable for deployment from vessels and can be easily configured for deployment from submersibles, making it compatible for use in areas with difficult access such as narrow canyons, highly energetic areas, and close offshore structures. As the *blueDrop* penetrates into sediments, its deceleration time history is recorded by the embedded accelerometer; the stiffness of the sediment can be assessed by analyzing the recorded deceleration vs. depth.

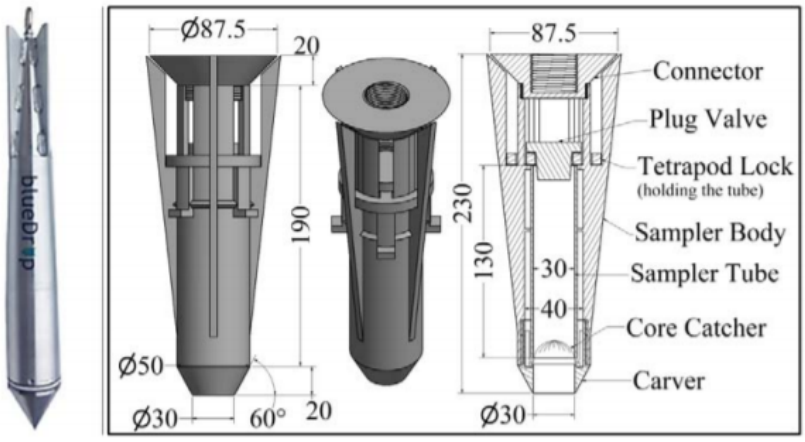

Figure 28: BuleDrop penetrometer (Stark, 2016) (unit: mm).

This section shows the simulations of the three penetrometer tests conducted on loose, medium, and dense sediments in the laboratory (in collaboration with Dr. Nina Stark from Virginia Tech). Figure 29 shows the setup. The container was transparent and had a length of 1.2 m, a width of 1.2 m, and a height of 1.0 m; the penetrometer had a total length of 0.631 m and a weight of 7.372 kg. The depth of the fluid and sediment was 0.4 m and 0.2 m, respectively. The release height of the penetrometer was slightly different among the three tests. As the penetrometer was released, its deceleration time history was recorded by the embedded accelerometer; its vertical velocity time history was obtained from its vertical position vs. time recorded by a high-speed camera.

The penetrometer tests were simulated using the model developed in this work. Figure 30 shows different

stages of a typical simulation. The main parameters used in the simulations are summarized in Table 3. The drop height was from the experiments; the bulk density, E_y, ν_p, c, and ϕ_0 were typical values based on the consistency of the sediments; and $\tilde{m}$, $\tilde{n}$ were calibrated against the test results. To demonstrate the calibration process, Figure 31 shows the effect of m on the simulation results using the experiment involving loose sediment as an example. Figure 31 indicates that $\tilde{m}$ has a negligible effect on the model simulation, hence a value of 100 is used for all three cases.

Table 3: Parameters for penetration simulation.

Case	$E_y(MPa)$	ν_p	$c(KPa)$	$\phi_0(\circ)$	$\tilde{m}$	$\tilde{n}$	bulk density	drop height (m)
Loose	20	0.48	1	30	100	1	1900 kg/m^3	1.3548
Medium	40	0.48	1	33	100	1	2000 kg/m^3	1.3827
Dense	60	0.48	1	36	100	1	2100 kg/m^3	1.3836

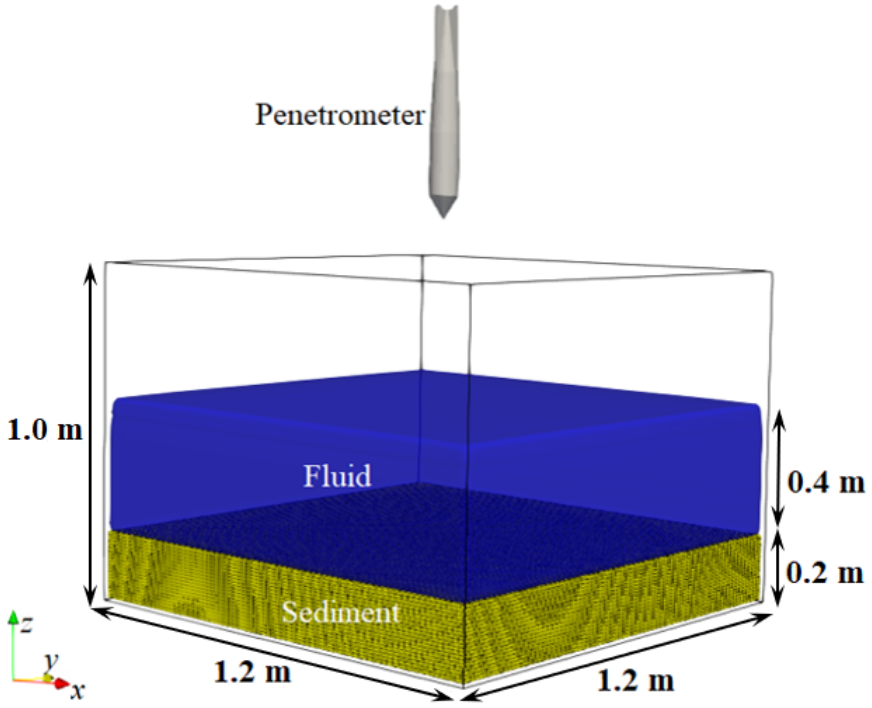

Figure 29: Case setup for the penetrometer simulation.

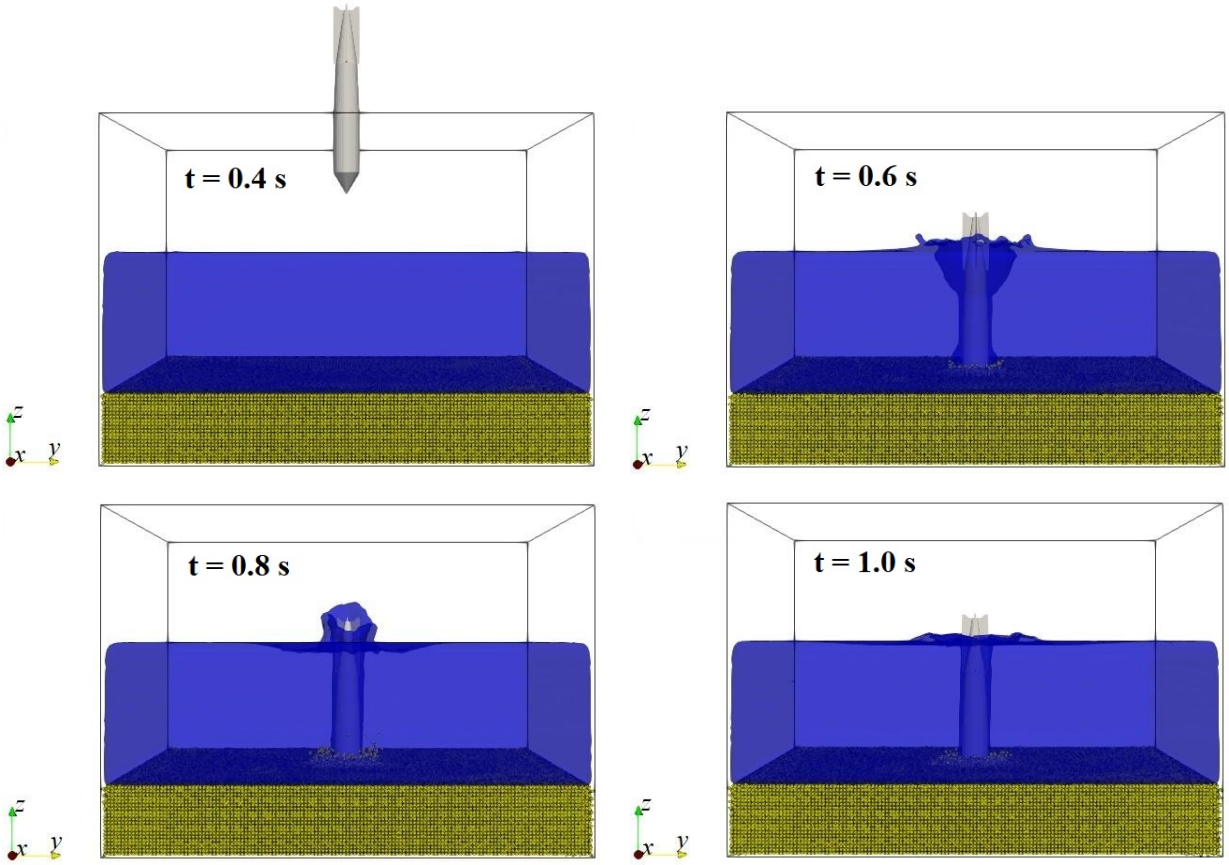

Figure 30: Simulation of dropping penetrometer into loose sediments.

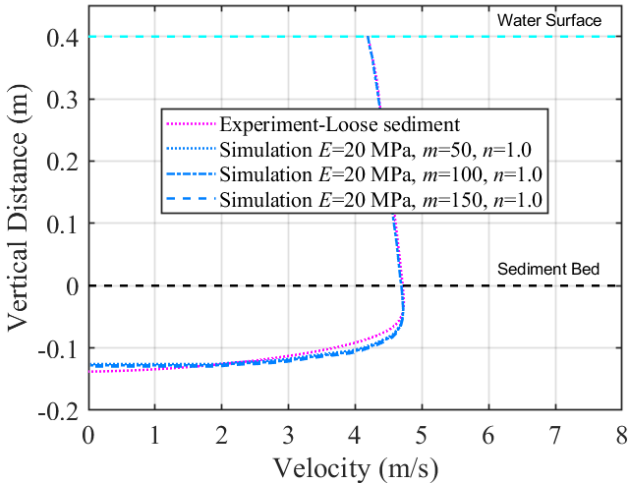

Figure 31: Effect of the parameter $\tilde{m}$ on simulation results (loose sediment).

The effects of two key parameters, E_y and $\tilde{n}$, on the simulation results are discussed below. The definitions of inflection depth and penetration depth of the penetrometer are shown in Figure 32. The inflection depth is defined when the velocity of the penetrometer reaches its maximum value in the sediment layer whereas the penetration depth is defined when the velocity of the penetrometer reaches zero. Figure 33a plots the effect of E_y, which controls the stiffness of the sediment in the elastic solid state, on the simulation results

for the loose sediment case. It is clearly shown that as the value of E_y increases and the sediment becomes stiffer, the penetration depth decreases. Figure 33a shows that E_y = 20 MPa results in the best overall match with the experimental observations in terms of the inflection and penetration depths; hence, this value is used (see Table 3). The E_y values for the medium and dense sediment cases are similarly obtained and the results are shown in Figure 34a and Figure 35a, respectively.

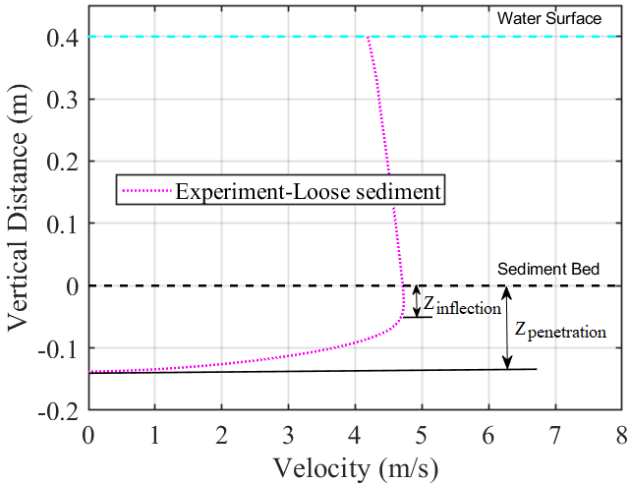

Figure 32: Definition of inflection and penetration depth of the penetrometer.

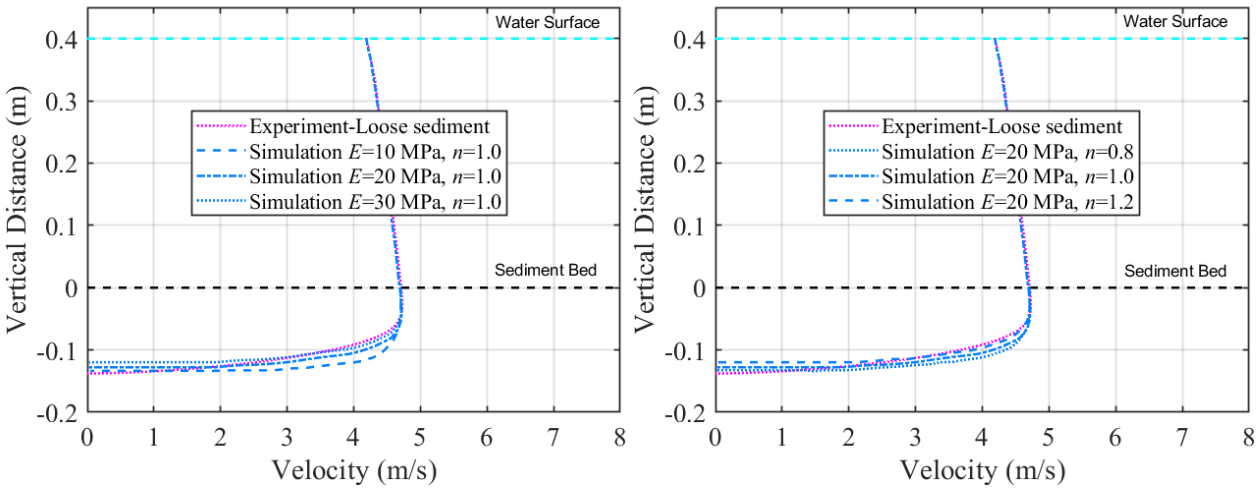

(a) Effect of E_y on simulation results

(b) Effect of $\tilde{n}$ on simulation results

Figure 33: Effects of E_y and $\tilde{n}$ on simulation results (loose sediment)

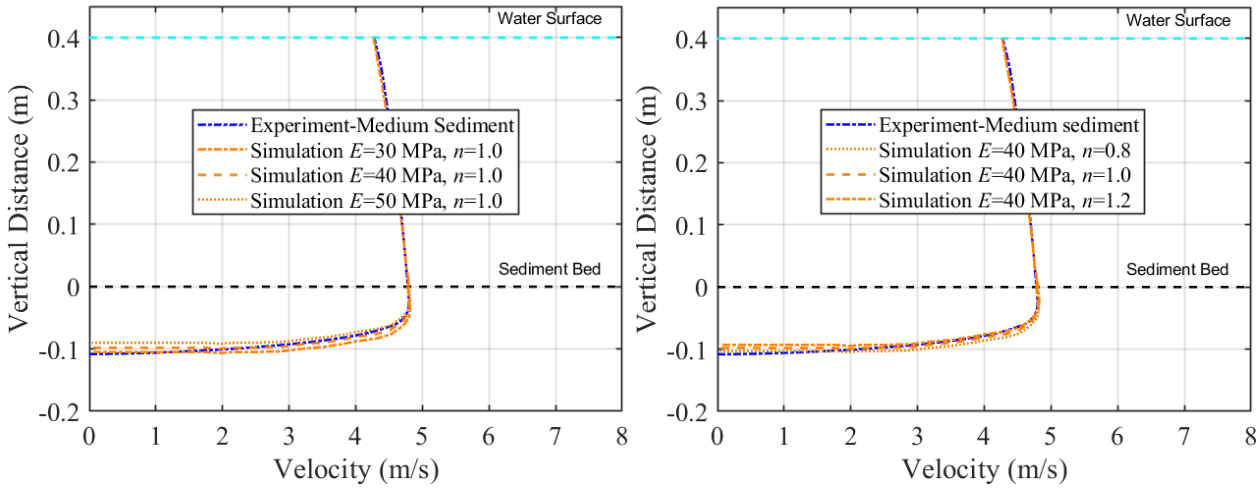

(a) Effect of E_y on simulation results

(b) Effect of $\tilde{n}$ on simulation results

Figure 34: Effects of E_y and $\tilde{n}$ on simulation results (medium sediment)

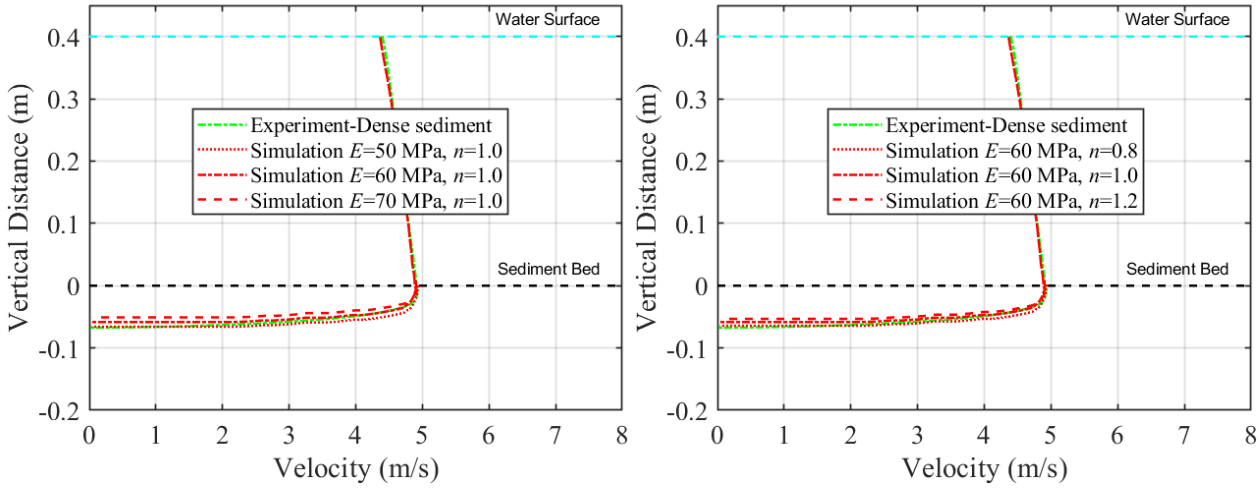

(a) Effect of E_y on simulation results

(b) Effect of $\tilde{n}$ on simulation results

Figure 35: Effects of E_y and $\tilde{n}$ on simulation results (dense sediment)

After the E_y values are fixed in all three cases, the effect of $\tilde{n}$ on the simulation results is studied. The power-law index $\tilde{n}$ controls the visco-plastic fluid state of the sediment. Figure 33b shows that for a given E_y value, the penetration depth increases as $\tilde{n}$ decreases. Figure 33b shows that $\tilde{n}$ = 1.0 results in the best overall match with the experimental observations in terms of the inflection and penetration depths; hence, this value is used (see Table 3). Comparing Figure 33a with Figure 33b, it is evident that E_y has a bigger influence on the simulation results than $\tilde{n}$; therefore, a constant $\tilde{n}$ value is used for all cases. Another rationale for this simplified treatment is that in the visco-plastic fluid state of the sediment, a significant deformation has accumulated and the effect of initial density of the sediment is likely erased, which is similar to the concept of critical state soil mechanics. Figure 36 summarizes the effects of E_y and $\tilde{n}$ on the inflection depth of the penetrometer. Figure 36 indicates that the inflection depth decreases as the relative

density of sediment increases from loose to dense, E_y increases, and $\tilde{n}$ increases. Again, the effect of $\tilde{n}$ on the inflection depth is relatively insignificant.

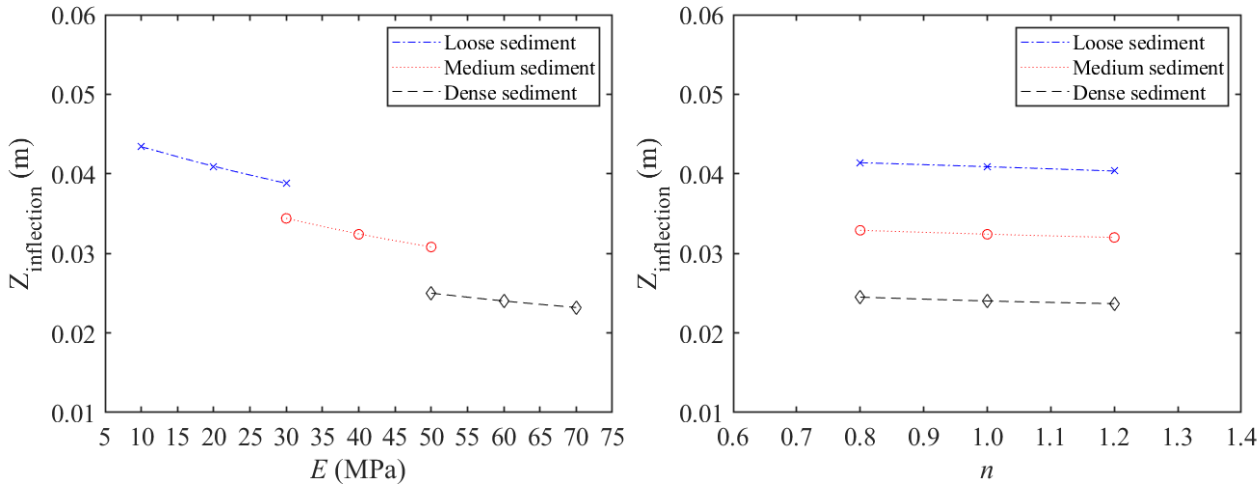

(a) Effect of E_y on simulation results

(b) Effect of $\tilde{n}$ on simulation results

Figure 36: Effect of E_y and $\tilde{n}$ on inflection depth.

Apart from the velocity, the deceleration, which is normalized by the gravity acceleration g, of the penetrometer was also studied. For all three cases (loose, medium, and dense sediment), the deceleration of the penetrometer undergoes the following process: gradually decreases, then gradually increases to its maximum value, and finally abruptly decreases to zero. The definition of stop depth of the penetrometer is shown in Figure 37, in which the stop depth is the depth penetrometer travels when its deceleration decrease from the maximum value to zero. Figure 38a plots the effect of E_y on the simulation results and indicates that as E_y increases the maximum value of the deceleration also increases. As to the effect of $\tilde{n}$ on the deceleration of the penetrometer, which is shown in Figure38b, similar conclusion can be drawn. In addition, when comparing with all three cases (see Figures 38, 39, and 40), the maximum value of the penetrometer's deceleration increases when the sediment becomes denser. This makes sense because when the sediment becomes denser the penetrometer will be more easily and quickly stopped.

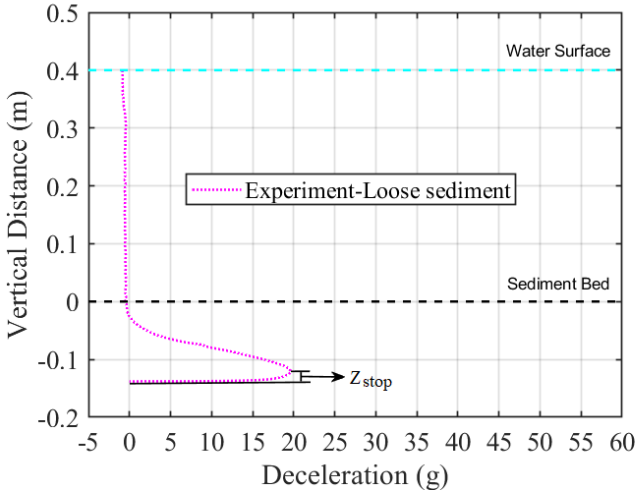

Figure 37: Definition of stop depth.

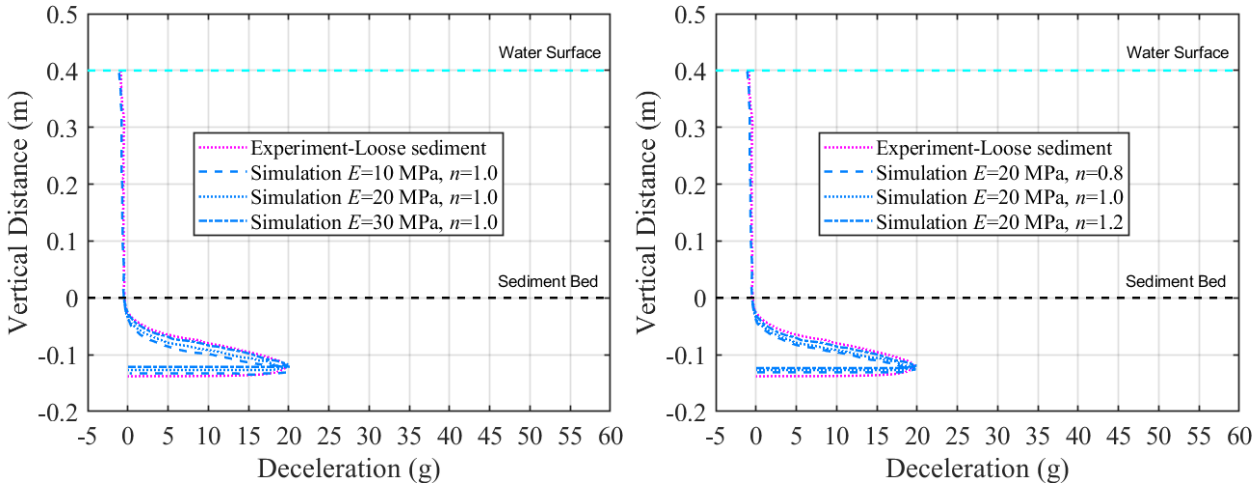

(a) Effect of E_y on simulation results

(b) Effect of $\tilde{n}$ on simulation results

Figure 38: Effect of E_y and $\tilde{n}$ on simulation results. (loose sediment)

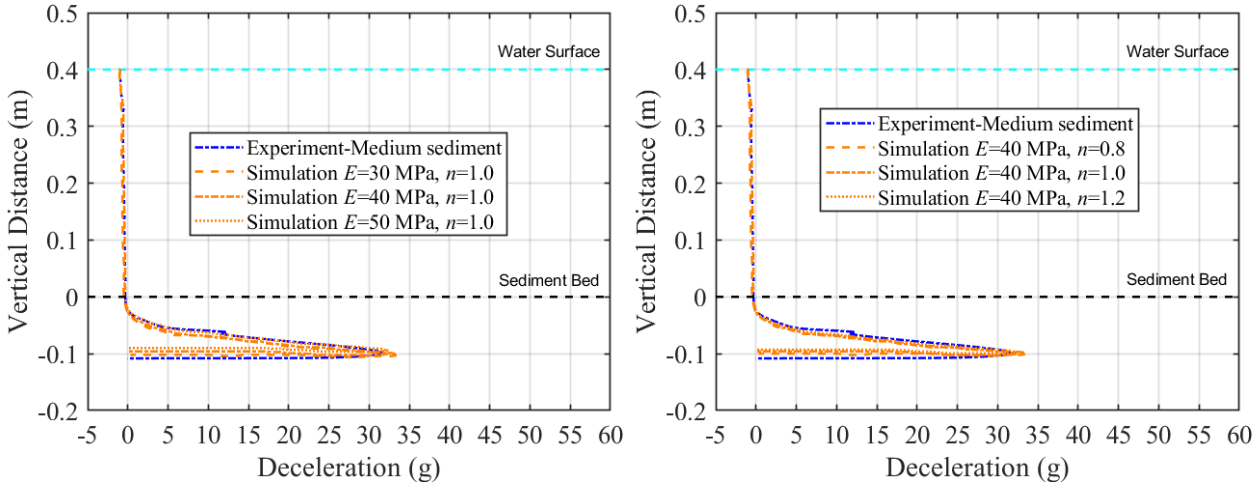

(a) Effect of E_y on simulation results

(b) Effect of $\tilde{n}$ on simulation results

Figure 39: Effect of E_y and $\tilde{n}$ on simulation results. (medium sediment)

Figure 41 summarizes the effect of E_y and $\tilde{n}$ on the stop depth. It clearly shows that in the stop phase, effect of E_y on the stop depth is very minimal since the stop depth line is almost flat when changing the value of E_y. While $\tilde{n}$ has a larger effect on the stop depth when compared with E_y, it indicates that $\tilde{n}$ plays an important role in the stop phase. The rationale behind this is that $\tilde{n}$ controls the visco-plastic fluid state of the sediment, and the stop phase falls into this state.

One important advantage of the developed SPH model is that it can calculate the time history of the force experienced by the munition. It is an important quantity which is hard to measure in experiments. In addition, the force acting on the object from different phases (water and sediment) can be calculated separately and their relative contribution can be analyzed. Figures 42, 43, and 44 plot the forces from water

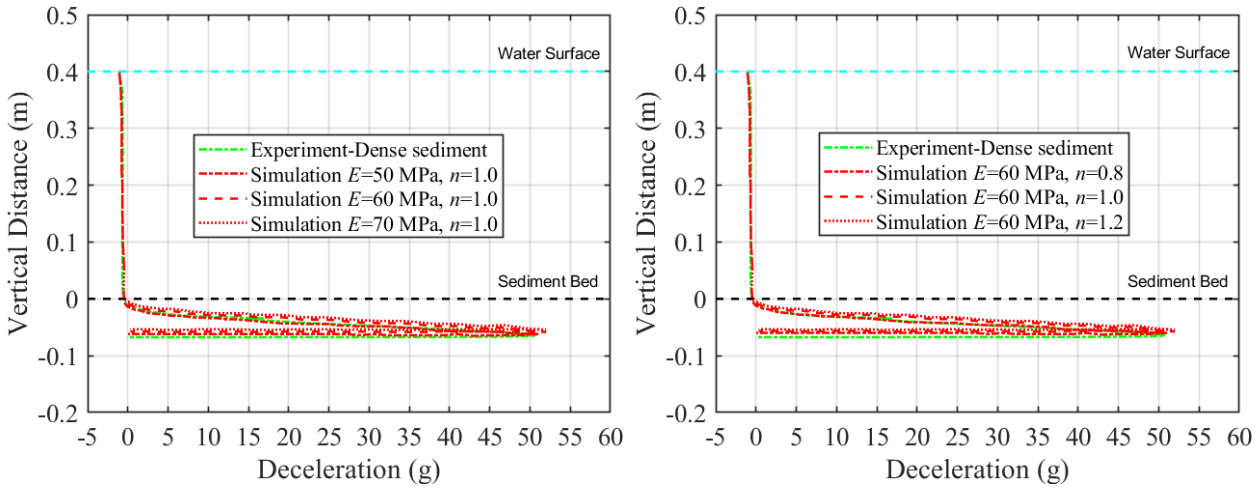

(a) Effect of E_y on simulation results

(b) Effect of $\tilde{n}$ on simulation results

Figure 40: Effect of E_y and $\tilde{n}$ on simulation results. (dense sediment)

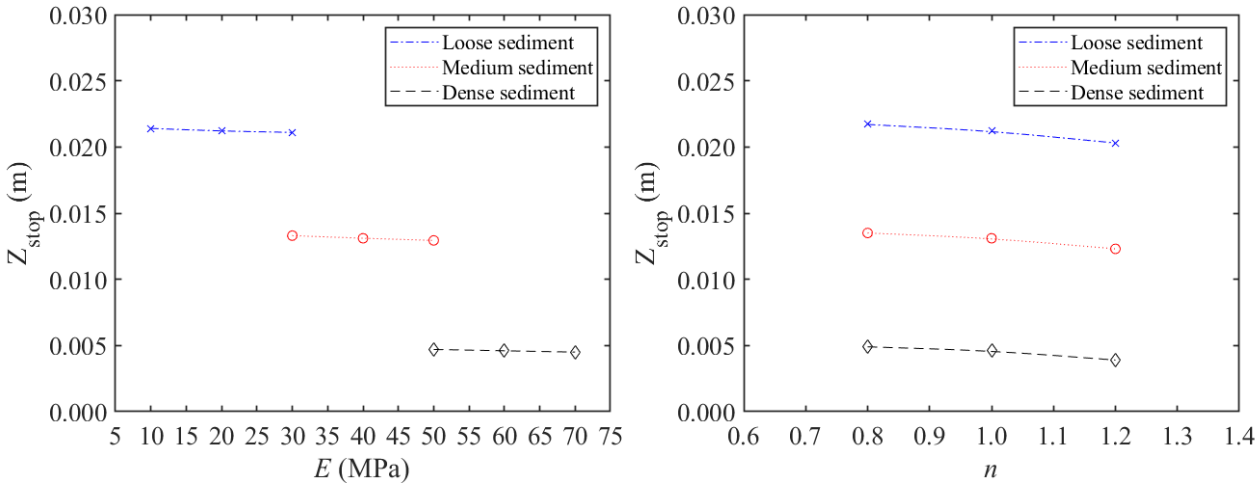

(a) Effect of E_y on simulation results

(b) Effect of $\tilde{n}$ on simulation results

Figure 41: Effect of E_y and $\tilde{n}$ on penetration depth.

(Fw) and sediment (Fs) acting on the penetrometer. It clearly shows that forces in z direction is dominant when compared with the other two components. This is of course due to the fact that the object falls freely into a tank with still water. Also, when the penetrometer approximately touches the water at 0.43 s and touches the sediment at 0.54 s, both forces from water and sediment in z direction increases abruptly. After the touching time, the forces from water and sediment in x and y directions only begin to fluctuate. It is found that the vertical force reaches its maximum approximately at the time the penetrometer touches the interface (either water or sediment). After these moments, both forces in z direction decrease and then reach a steady state, which corresponds to the time when the penetrometer totally stops and the vertical supporting force is balanced by the constant gravity force. Comparing Figures 42, 43, and 44, one can conclude that the magnitude of force from the sediment increases with the increase of E_y. This is because larger E_y makes the sediment stiffer. The magnitude of force from water do not vary too much because the drop height for three cases is almost the same.

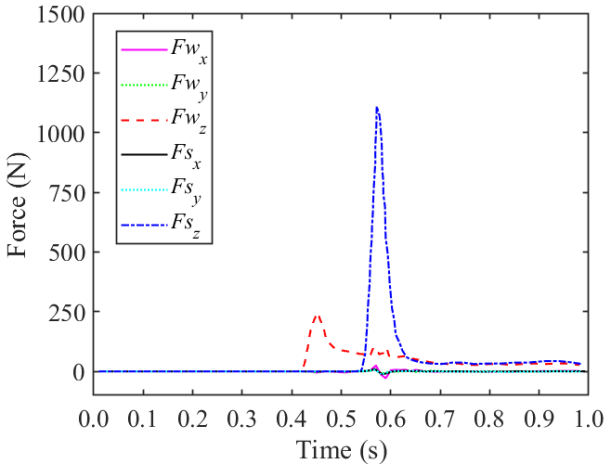

Figure 42: Forces acting on the penetrometer (loose sediment).

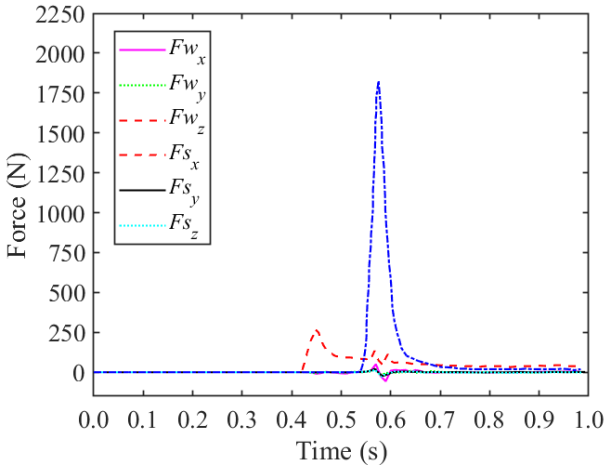

Figure 43: Forces acting on the penetrometer (medium sediment).

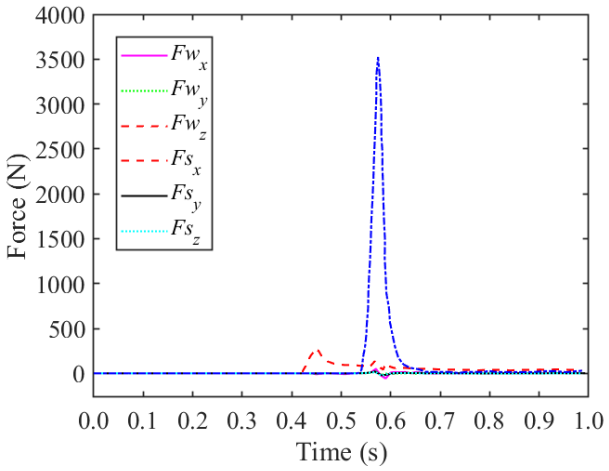

Figure 44: Forces acting on the penetrometer (dense sediment).

4.2.3 Simulation results of cohesive soil

Underwater environment may include cohesive soil and its interaction with munitions is of interest. In this section, to demonstrate the capability of the SPH model for soil cohesion, the case of cohesive soil collapse, also known as "slump test" is simulated. The goal is to study the rheology of soil masses involved in flow-slides. In particular, the final run-out distance and deposit profile are studied by varying sediment properties and initial setup of the slump. Two cases are simulated by changing the initial aspect ratio. Table 4 summarizes the parameters used in the simulation of cohesive soil. This case is a simple demonstration.

Table 4: Parameters for simulation of cohesive soil.

Case	$E_y(MPa)$	ν_p	$c(KPa)$	$\phi_0(\circ)$	$\tilde{m}$	$\tilde{n}$	μ	bulk density	inital aspect ratio
a	0.5	0.48	2	10	100	1.2	0.002	1505.1 kg/m^3	1.88
b	0.5	0.48	2	10	100	1.2	0.002	1505.1 kg/m^3	2.82

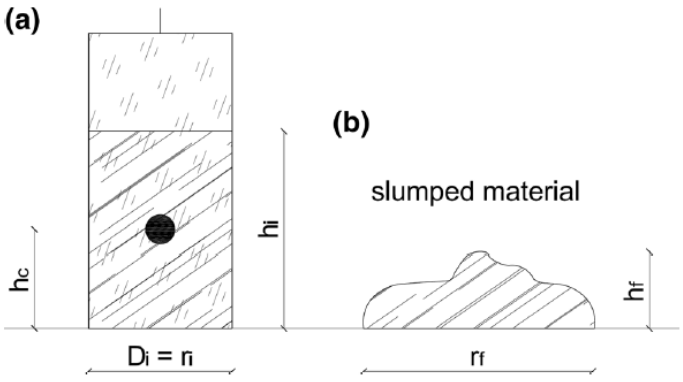

Figure 45: Cohesive sediment case: (a) initial profile of the collapsing mass; (b) final profile of the collapsing mass (Brezzi et al., 2018).

The setup of cohesive soil simulation for two different initial aspect ratios is shown in Figure 46. The

final run-out distance , height and deposit profile for these two cases are studied and compared with the experiment of Brezzi et al. (2018). Note that the final run-out distance and height are both normalized by the initial run-out distance D_i. Comparing Figure. 48a and 48b, it can be concluded when comparing with the experimental result the error of final run-out distance is larger than the final height. But for both cases, the final run-out distance and height are overestimated by the present model. Further calibration on the model parameters is needed.

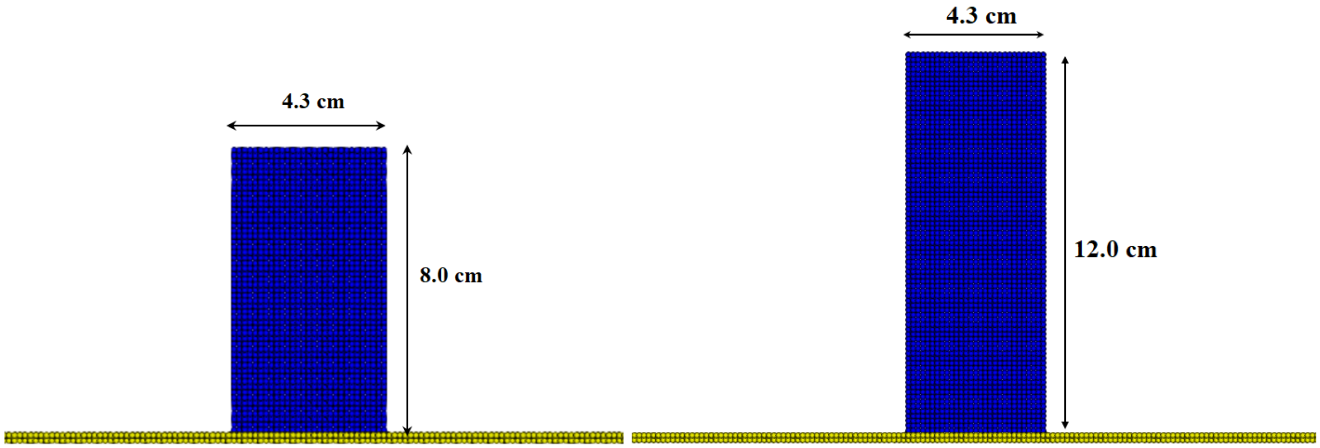

(a) Initial aspect ratio = 1.88 (b) Initial aspect ratio = 2.82

Figure 46: Initial setup of cohesive soil.

(a) Final profile for initial aspect ratio = 1.88 (b) Final profile for initial aspect ratio = 2.82

Figure 47: Final profile of cohesive soil.

4.2.4 Munition mobility under cyclic loading

There is a consensus in the munition response research community that munition density is the key parameter for its mobility. However, experiments can only show its importance phenomenologically. With the 3D SPH model developed in this work, it is possible to make quantitative analysis.

In this section, munition object is placed underwater and above the sediment bed. The whole system is a closed box. A cyclic loading is applied to "shake" the system. As shown in experiments, the munition's movement depends on its relative density with respect to the sediment. Light munition will stay on top of sediment while heavy ones will sink into the bed. By changing the relative density (munition density relative to the sediment density), three cases were simulated. Parameters for cases are listed in Table 5.

Figure 49 shows the simulated final position of the munition which indeed demonstrates the importance

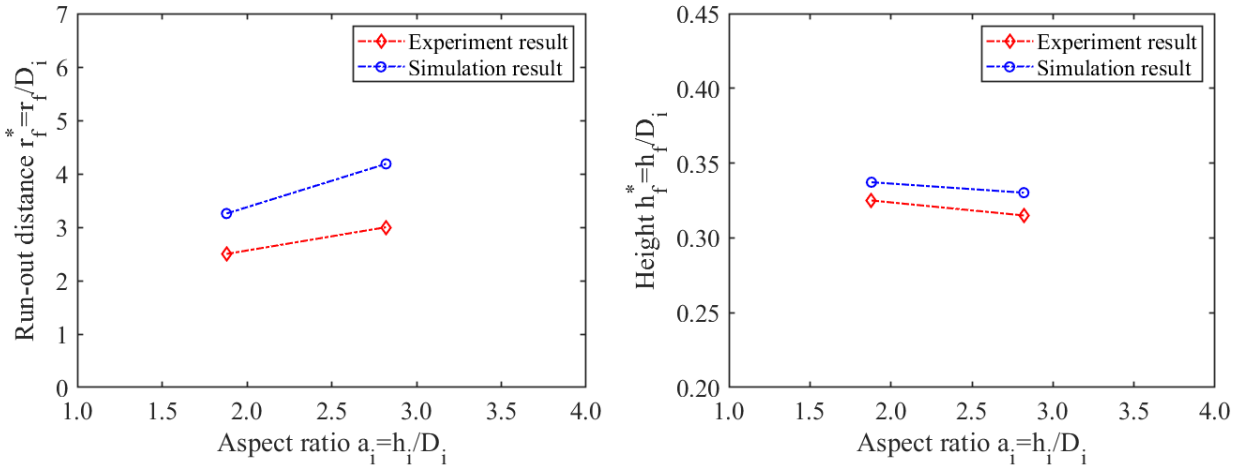

(a) Final run-out distance

(b) Final height

Figure 48: Final run-out distance and height of cohesive soil.

of relative density of munitions. In case (a), see Figure 49a, a munition with small density is initially put at the bottom of the tank. When a cyclic loading (in x direction) is acted on the tank, the munition continuously floats up until it arrives at the surface of the sediment bed. In case (b), see Figure 49b, under the same loading, the munition has a medium density and is initially placed on the sediment bed. The simulation shows that the munition stays at the sediment bed. In case (c), see Figure 49c, its setup is the same as case (b) except that the munition has a larger density. The munition sinks down to the sediment as expected.

Table 5: Parameters for munition mobility under cyclic loading.

Case	$E_y(MPa)$	ν_p	$c(KPa)$	$\phi_0(\circ)$	$\tilde{m}$	$\tilde{n}$	μ	frequency	amplitude	relative density
a	20	0.48	0.5	30	100	1.2	0.002	3 Hz	5 cm	0.45
b	20	0.48	0.5	30	100	1.2	0.002	3 Hz	5 cm	1.51
c	20	0.48	0.5	30	100	1.2	0.002	3 Hz	5 cm	2.97

With the 3D SPH model, it is also possible to extract the forces on the object and analyze the cause of different behavior of munition. Figure 50 plots the forces acting on the munition for the three cases. It shows that for all three cases, the force in the x direction Fx has a sinusoidal shape which is because the cyclic loading is applied in the x direction. In the vertical y direction, the force history depends on the motion and position of the munition. For case (b), the vertical force oscillates in more chaotic fashion because it keeps its location at approximate the sediment-water interface.

4.2.5 Simulation of munition dynamics under dam break waves

This case is more close to reality. It simulates the lab experiment performed at the University of Delaware (in collaboration with Dr. Jack Puleo). In the experiment, the motion of an object (surrogates for UXOs) on a sloping sediment beach under the action of dam break wave is studied. Detailed measurements on free surface dynamics and turbulent flow have been provided to us. More data on scour and object motion trajectory will be available in the next phase of the project. Thus, this section does not contain comparison

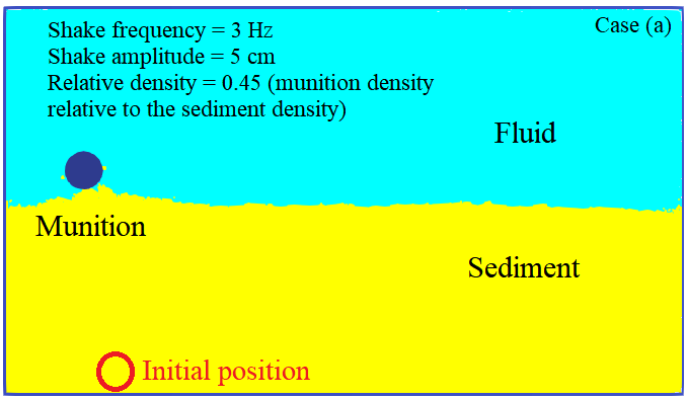

(a) Relative density = 0.45

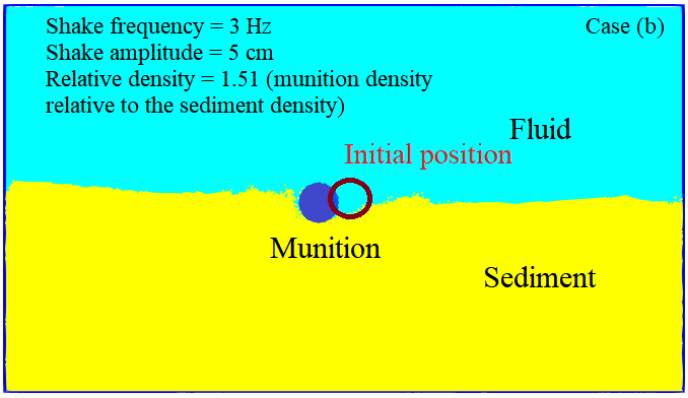

(b) Relative density = 1.51

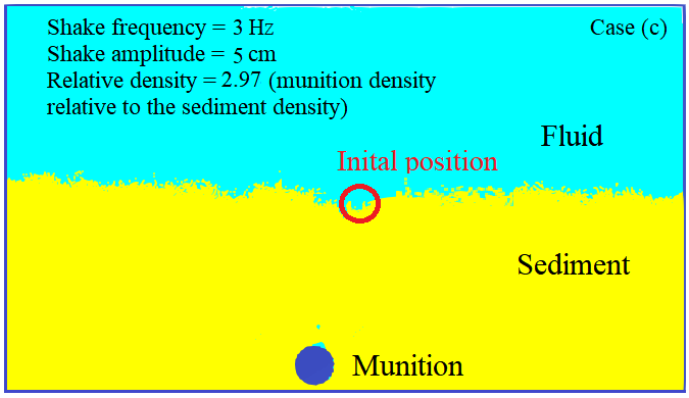

(c) Relative density = 2.97

Figure 49: Density effect on munition mobility.

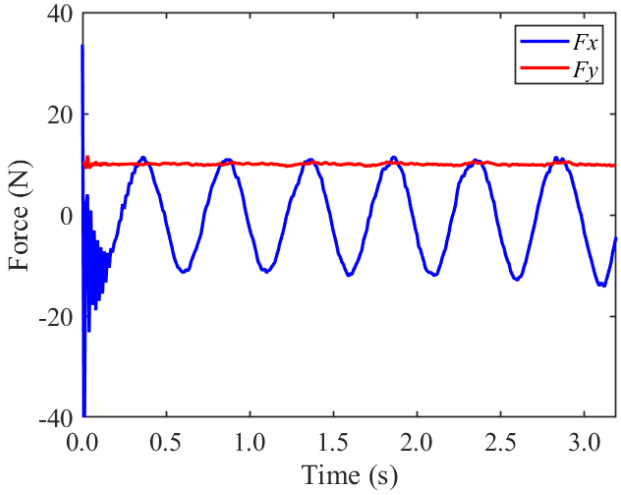

(a) Relative density = 0.45

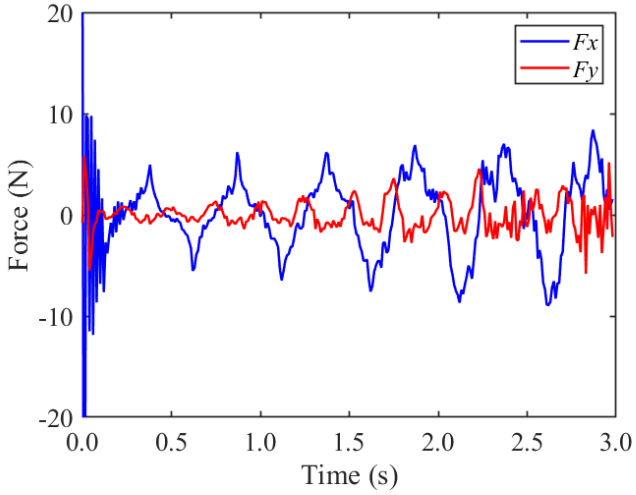

(b) Relative density = 1.51

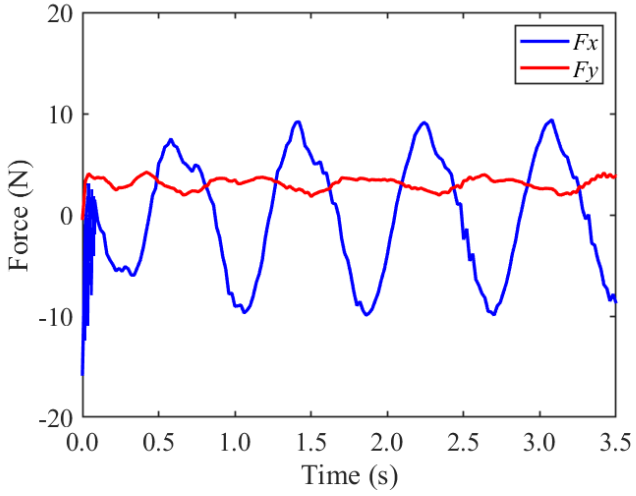

(c) Relative density = 2.97

Figure 50: Forces acting on the munition.

on scour and munition motion. Only a qualitative analysis is given. Case setup is shown in Figure 51 and parameters used in the simulation is listed in Table 6.

Table 6: Parameters for munition under dam break waves.

Case	$E_y(MPa)$	ν_p	$c(KPa)$	$\phi_0(\circ)$	$\tilde{m}$	$\tilde{n}$	μ	specific density
a	50	0.48	1	35	100	1.8	0.002	3.5

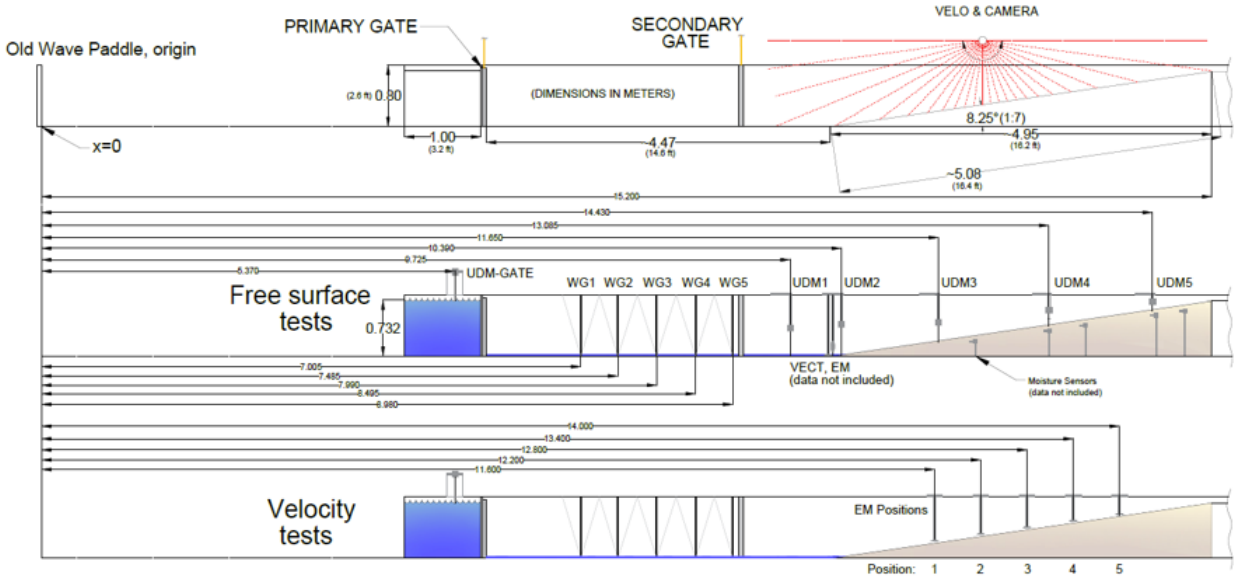

Figure 51: Simulation setup for munition under dam break waves.

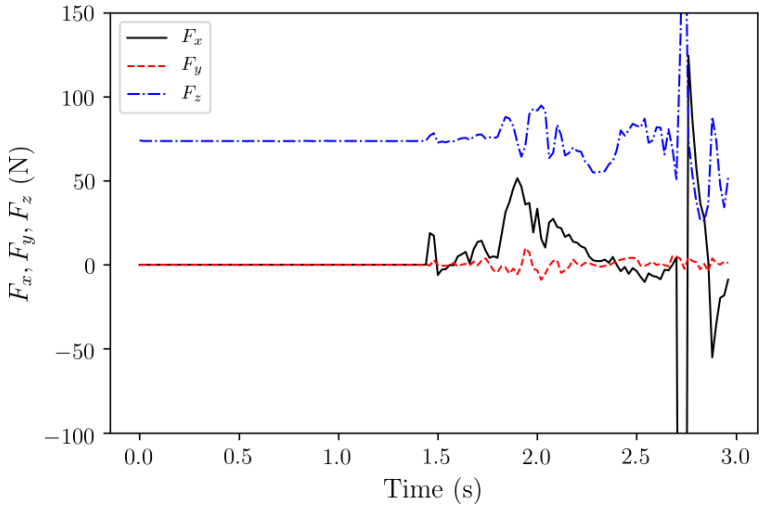

Figure 52: Forces acting on the munition.

Forces acting on the munition is plotted in Figure 52 and four representative times are selected to describe different wave stages the munition encounters (Figure 53). At $t = 1.2\ s$, dam break waves has not yet touched the munition and the only external force acting on the munition comes from the sediment supporting force F_z which is balanced by the munition gravity. At $t = 1.4\ s$, the dam break waves front arrives

at the munition and the horizontal force in the wave propagation direction F_x increases abruptly. At the same time, the munition starts to move due to wave impact. At $t = 1.8\ s$, F_x approaches its first maximum point. The munition keeps moving along with the wave until it hits the end wall. And at $t = 2.7\ s$, the munition collides with the rigid wall and the magnitude of F_x increases abruptly but in the negative x direction.

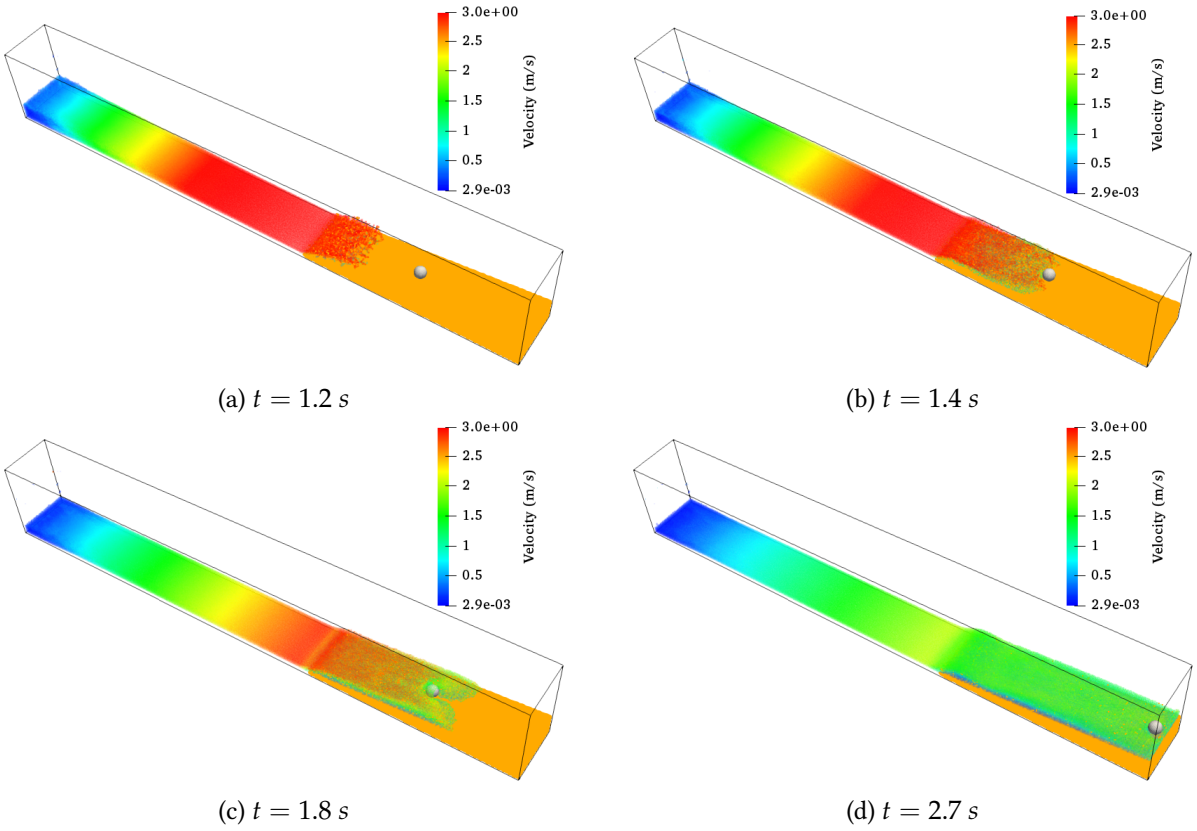

(a) $t = 1.2\ s$ (b) $t = 1.4\ s$

(c) $t = 1.8\ s$ (d) $t = 2.7\ s$

Figure 53: Munition mobility under dam break waves.

5 CONCLUSION TO DATE

The major accomplishment till this point is that the proposed computational model has been developed. This three-dimensional modeling framework captures the main physical processes controlling the dynamics of underwater munitions. These physical processes include turbulent flow, sediment transport and scour, granular material dynamics, the 6-DoF rigid body dynamics of munition, and the interactions among all the above. For such a complex dynamical system with three phases, i.e., flow, sediment, and munition, the technical approach proposed to make the problem tractable is to divide the domain into sub-domains based on the dominant physical processes. The major sub-domains include: (1) the CFD domain for flow and sediment transport, and (2) the SPH domain for granular material dynamics and munition's rigid body motion.

In the CFD domain, an accurate and robust IB method is applied and validated to solve the flow field and give smooth bed shear stress, which is the driver for sediment transport. The smoothness of bed shear stress is the result of a new IB method which adaptively adjust the location of IB cells such that its image point is in the log-law layer. The moving munition and deforming bed can be both modeled with the

IB method because they interact with each other. This is the great advantage of the new IB method in comparison with other methods such as the ALE method. In the 3D scour model, both suspended load and bedload are included and the Exner equation is used to update the bed elevation. To deal with the sand slide process, a new physically-based solution is proposed based on the similarity and difference between sand slide and diffusion processes. The model in the CFD domain is extensively validated for the hydrodynamics. Some scour and sediment transport validation has been done. All simulation cases show that the 3D scour model is capable of capturing the flow and sediment transport processes when the munition is fixed or moving.

In the SPH domain, the mixture of fluid and sediment is modeled as a two-phase fluid where the fluid phase is treated as simple Newtonian fluid and the sediment part is treated as granular material which has an isotropic linear behavior and obeys a yield criterion. The SPH model also solves the 6-DoF motion of object and its interaction with other phases. Several validation and demonstration cases have been shown. In the 2D sediment dam break case, by comparison with previous numerical models, it is shown that the model developed in this work makes good improvements. More specifically, the surface profile and yield region of the sediment showed better agreement with the experimental data. Satisfactory results are observed in the 3D penetrometer simulations where three cases for loose, medium, and dense sediment were studied. The penetration depth, velocity, and deceleration profiles of the penetrometer showed good agreement with the experimental results. It is found that the Young's modulus E_y plays an important role in the present multiphase model. When E_y increases, the inflection depth decrease. Also, although $\tilde{n}$ has a similar effect as E_y, E_y has a bigger impact than $\tilde{n}$. In particular, E_y approximately has a negatively linear relationship with the inflection depth, while the effect of $\tilde{n}$ is negligible. However, in the stopping phase, the effect of E_y on the stop depth of the penetrometer is very minimal when comparing with $\tilde{n}$. In addition, the maximum deceleration of the penetrometer is well predicted by the current model. Additional cases to demonstrate the capability of the model include the collapse of cohesive sediment, the mobility of munition under cyclic loading to show the effect of density, and the munition dynamics on sloping sediment beach under dam break wave action. All these cases show qualitatively good results and the unique information, for example, force history on munitions, provides an important window to unravel the complex dynamics governing the fate of underwater munitions.

6 Submitted/In-progress publications from this work

The following is a list of publications that are submitted or in progress:

- Y. Xu and X. Liu. An immersed boundary method with y^+-adaptation wall function for smooth wall shear. *Computers & Fluids*, 2019
- Z. Li, T. Qiu, G. Fourtakas, N. Stark, X. Liu. Dynamics of Coupled Flow-Object-Sediment Systems with Smoothed Particle Hydrodynamics (SPH) Simulations. *Acta Geotechnica*, 2019
- Y. Song, Y. Xu, and X. Liu. A gradient-limited diffusive sand slide method in scour models. *Journal of Hydraulic Engineering*, 2019

7 LITERATURE CITED

Batchelor, G. K. *An Introduction to Fluid Dynamics*. 2000. ISBN 9780511800955. doi: 10.1017/CBO9780511800955.

Brezzi, L., Gabrieli, F., and Cola, S. Collapse of granular-cohesive soil mixtures on a horizontal plane, 2018. ISSN 18611133.

Brørs, B. Numerical modeling of flow and scour at pipelines. *Journal of hydraulic Engineering*, 125(5): 511–523, 1999.

Bui, H. H., Fukagawa, R., Sako, K., and Ohno, S. Lagrangian meshfree particles method (SPH) for large deformation and failure flows of geomaterial using elastic-plastic soil constitutive model. *International Journal for Numerical and Analytical Methods in Geomechanics*, 2008. ISSN 03639061. doi: 10.1002/nag.688.

Chen, X., Li, Y., Niu, X., Li, M., Chen, D., and Yu, X. A general two-phase turbulent flow model applied to the study of sediment transport in open channels. *International Journal of Multiphase Flow*, 37(9): 1099–1108, 2011. ISSN 03019322. doi: 10.1016/j.ijmultiphaseflow.2011.05.013.

Crespo, A. J., Gómez-Gesteira, M., and Dalrymple, R. A. Boundary conditions generated by dynamic particles in SPH methods. *Computers, Materials and Continua*, 2007. ISSN 15462218.

Crespo, A. J., Domínguez, J. M., Rogers, B. D., Gómez-Gesteira, M., Longshaw, S., Canelas, R., Vacondio, R., Barreiro, A., and García-Feal, O. DualSPHysics: Open-source parallel CFD solver based on Smoothed Particle Hydrodynamics (SPH). *Computer Physics Communications*, 2015. ISSN 00104655. doi: 10.1016/j.cpc.2014.10.004.

Drucker, D. C. and Prager, W. Soil mechanics and plastic analysis or limit design. *Quarterly of Applied Mathematics*, 1952. ISSN 0033-569X. doi: 10.1090/qam/48291.

Engelund, F. and Fredsøe, J. A sediment transport model for straight alluvial channels. *Hydrology Research*, 7(5):293–306, 1976.

Fern, E. J. and Soga, K. The role of constitutive models in MPM simulations of granular column collapses. *Acta Geotechnica*, 2016. ISSN 18611133. doi: 10.1007/s11440-016-0436-x.

Fourtakas, G. and Rogers, B. D. Modelling multi-phase liquid-sediment scour and resuspension induced by rapid flows using Smoothed Particle Hydrodynamics (SPH) accelerated with a Graphics Processing Unit (GPU). *Advances in Water Resources*, 2016. ISSN 03091708. doi: 10.1016/j.advwatres.2016.04.009.

Fourtakas, G., Rogers, B. D., and Laurence, D. R. Modelling sediment resuspension in industrial tanks using SPH. *La Houille Blanche*, 2013. ISSN 0018-6368. doi: 10.1051/lhb/2013014.

Ghaïtanellis, A., Violeau, D., Ferrand, M., Abderrezzak, K. E. K., Leroy, A., and Joly, A. A SPH elastic-viscoplastic model for granular flows and bed-load transport. *Advances in Water Resources*, 2018. ISSN 03091708. doi: 10.1016/j.advwatres.2017.11.007.

Gilmanov, A. and Sotiropoulos, F. A hybrid Cartesian/immersed boundary method for simulating flows with 3D, geometrically complex, moving bodies. *J Comput Phys*, 207(2):457–492, 2005. ISSN 00219991.

Gilmanov, A., Le, T. B., and Sotiropoulos, F. A numerical approach for simulating fluid structure interaction of flexible thin shells undergoing arbitrarily large deformations in complex domains. *J Comput Phys*, 300:814–843, 2015. ISSN 10902716.

Gomez-Gesteira, M., Rogers, B. D., Crespo, A. J., Dalrymple, R. A., Narayanaswamy, M., and Dominguez, J. M. SPHysics - development of a free-surface fluid solver - Part 1: Theory and formulations. *Computers and Geosciences*, 2012. ISSN 00983004. doi: 10.1016/j.cageo.2012.02.029.

Jasak, H. and Tuković, Ž. Immersed Boundary Method in FOAM — Theory, Implementation and Use (Presentation slides), 2015.

Jasak, H., Rigler, D., and Tuković, Ž. Design and implementation of Immersed Boundary Method with discrete forcing approach for boundary conditions. In *11th World Congr Comput Mech WCCM 2014, 5th Eur Conf Comput Mech ECCM 2014 6th Eur Conf Comput Fluid Dyn ECFD 2014*, 2014. ISBN 9788494284472.

Li, Z. A fast iterative algorithm for elliptic interface problems. *J. Numer. Anal.*, 35(1):230–254, 1998.

Liu, M. B. and Liu, G. R. Smoothed Particle Hydrodynamics (SPH): an Overview and Recent Developments. *Arch Comput Methods Eng*, 17:25–76, 2010. doi: 10.1007/s11831-010-9040-7.

Lube, G., Huppert, H. E., Sparks, R. S. J., and Hallworth, M. A. Axisymmetric collapses of granular columns. *Journal of Fluid Mechanics*, 508:175–199, 2004.

Mast, C. M., Arduino, P., Mackenzie-Helnwein, P., and Miller, G. R. Simulating granular column collapse using the Material Point Method. *Acta Geotechnica*, 2014. ISSN 18611133. doi: 10.1007/s11440-014-0309-0.

Mittal, R. and Iaccarino, G. Immersed boundary methods. *Annu Rev Fluid Mech*, 37(1):239–261, 2005. ISSN 0066-4189.

Molteni, D. and Colagrossi, A. A simple procedure to improve the pressure evaluation in hydrodynamic context using the SPH. *Computer Physics Communications*, 2009. ISSN 00104655. doi: 10.1016/j.cpc.2008.12.004.

Monaghan, J. J. On the problem of penetration in particle methods. *Journal of Computational Physics*, 1989. ISSN 10902716. doi: 10.1016/0021-9991(89)90032-6.

Monaghan, J. J. SPH without a Tensile Instability. *Journal of Computational Physics*, 2000. ISSN 00219991. doi: 10.1006/jcph.2000.6439.

Monaghan, J. J. Smoothed particle hydrodynamics, 2005. ISSN 00344885.

OpenCFD, . OpenFOAM: The Open Source Computational Fluid Dynamics (CFD) Toolbox. http:://www.OpenFoam.org, 2019.

Papanastasiou, T. C. Flows of Materials with Yield. *Journal of Rheology*, 2002. ISSN 0148-6055. doi: 10.1122/1.549926.

Parker, G., Toro-Escobar, C. M., Ramey, M., and Beck, S. Effect of floodwater extraction on mountain stream morphology. *Journal of Hydraulic Engineering*, 129(11):885–895, 2003.

Pitz, R. and Daily, J. Experimental study of combustion in a turbulent free shear layer formed at a rearward facing step. In *19th Aerosp Sci Meet*, 1981.

Roman, F., Armenio, V., and Fröhlich, J. A simple wall-layer model for large eddy simulation with immersed boundary method. *Physics of Fluids*, 21(10):101701, 2009. ISSN 10706631. doi: 10.1063/1.3245294.

Roulund, A., Sumer, B. M., Fredsøe, J., and Michelsen, J. Numerical and experimental investigation of flow and scour around a circular pile. *Journal of Fluid Mechanics*, 534:351–401, 2005.

Seo, J. H. and Mittal, R. A high-order immersed boundary method for acoustic wave scattering and low-Mach number flow-induced sound in complex geometries. *J Comput Phys*, 230(4):1000–1019, 2011. ISSN 00219991.

Singh, J., Altinakar, M. S., and Ding, Y. Numerical Modeling of Rainfall-Generated Overland Flow Using Nonlinear Shallow-Water Equations. *Journal of Hydrologic Engineering*, 20(8):4014089, 2015. ISSN 1084-0699. doi: 10.1061/(ASCE)HE.1943-5584.0001124.

Stark, N. Geotechnical site investigation in energetic nearshore zones: Opportunities & challenges. *Australian Geomechanics Journal*, 2016. ISSN 08189110.

Ulrich, C., Leonardi, M., and Rung, T. Multi-physics SPH simulation of complex marine-engineering hydrodynamic problems. *Ocean Engineering*, 2013. ISSN 00298018. doi: 10.1016/j.oceaneng.2013.02.007.

Rijn, L. C.van . Sediment transport, part II: suspended load transport. *Journal of hydraulic engineering*, 110 (11):1613–1641, 1984.

Vand, V. Viscosity of solutions and suspensions. I: Theory. *Journal of Physical and Colloid Chemistry*, 1948. ISSN 00223654. doi: 10.1021/j150458a001.

Violeau, D. *Fluid Mechanics and the SPH Method: Theory and Applications*. 2012. ISBN 9780191741227. doi: 10.1093/acprof:oso/9780199655526.001.0001.

Wilcox, D. C. *Turbulence Modeling for CFD*. DCW Industries, Inc., La Canada CA, 3rd editio edition, 2006.

Zhang, X., Krabbenhoft, K., and Sheng, D. Particle finite element analysis of the granular column collapse problem. *Granular Matter*, 2014. ISSN 14347636. doi: 10.1007/s10035-014-0505-5.